# Quantitative Comparison and Analysis of Different Power Routing Methods for Single-Phase Cascaded H-Bridge Photovoltaic Grid-Connected Inverter

Siwei Yang, Xing Zhang, *Senior Member, IEEE*, Wang Mao, Yuhua Hu, Mingda Wang, Fusheng Wang, *Member, IEEE*, and Renxian Cao

***Abstract*—The output power of each photovoltaic (PV) module is different in the single-phase cascaded H-bridge (CHB) PV grid-connected inverter due to irradiance intensity, ambient temperature, and aging degree of PV modules. When the PV modules are operating at their respective maximum power points, the corresponding dc-side voltages of the H-bridge units drift due to uneven power distribution, which will cause the maximum power point tracking failure. As a result, the grid current will deteriorate and even the system will become unstable. The power routing control methods based on fundamental voltage reconstruction, third harmonic injection and hybrid pulse width modulation can realize unequal power distribution between H-bridges to ensure the system stable operation. This article summarizes the abovementioned typical power routing control methods, derives the expressions of power routing ranges of different methods, then comprehensively and deeply compares the power routing capabilities of various methods qualitatively and quantitatively. The simulation results of a single-phase seven-level CHB PV grid-connected inverter demonstrate the validity of the theoretical analyses.**

***Index Terms*—Cascaded H-bridge (CHB), photovoltaic (PV) inverter, power routing methods, quantitative comparison.**

## I. Introduction

As THE continuous development and utilization of renewable energy, photovoltaic (PV) power generation technology and equipment are becoming increasingly mature. Compared with traditional two-level inverters, cascaded H-bridge (CHB) PV inverters have the advantages of easy modular expansion, multilevel output voltage, low switching frequency, high conversion efficiency, etc. [1]–[3]. More importantly, each H-bridge power unit in the CHB inverter requires an independent dc power supply, which is in line with the characteristics of PV array power generation. Therefore, the CHB inverter has significant advantages in PV power generation applications [4]–[6].

In the single-phase CHB PV inverter, the output power of each PV module is different due to factors such as light intensity, ambient temperature, and aging degree of PV modules, resulting in different ac output power of each H-bridge unit. When the PV module is operating at its maximum power point, the corresponding dc-side voltage of each H-bridge unit will drift due to uneven power distribution. The voltage drift causes the output voltage of the PV module to deviate from its maximum power point voltage, which in turn causes maximum power point tracking (MPPT) failure. Eventually, the grid current performance of the inverter deteriorates and even the system becomes unstable [7], [8].

Aiming at the unequal power distribution problem of single-phase CHB PV grid-connected inverters, Ko *et al.* [9], Liserre *et al.* [10], Raveendran *et al.* [11], Buticchi *et al.* [12], Andresen *et al.* [13], and Raveendran *et al.* [14], [15] proposed a concept of power routing to solve the unstable problem because of different power distribution in each H-bridge. Lots of literatures have proposed a variety of power routing control methods as follows. A power routing control method based on fundamental voltage reconstruction is proposed in [16]–[26], which means that the active component of the output voltage of each H-bridge unit is distributed in proportion to its dc-side input power. In detail, according to the way of reactive power distribution, they can be divided into three categories, which are: the system reactive power is distributed by each H-bridge unit in proportion to their dc-side input power [16]–[20], the system reactive power is undertaken by the specific H-bridge unit [21]–[23], and the system reactive power is distributed by each H-bridge unit equally [24]–[26]. However, although the abovementioned methods can achieve unequal power distribution between H-bridge units, their power routing ranges are small [27]. In order to further expand the power routing range, Ko *et al.* [28] proposed a third harmonic injection method. It makes the modulation degree of some H-bridge units with large output power reach 1.155, which improves the dc-side voltage utilization. Based on the [28],

Manuscript received April 30, 2020; revised June 27, 2020 and August 17, 2020; accepted September 11, 2020. Date of publication September 15, 2020; date of current version November 20, 2020. This work was supported in part by the National Key R&D Program of China under Grant 2018YFB1500703, and in part by the Fundamental Research Funds for the Central Universities of China under Grant PA2019GDPK0080. Recommended for publication by Associate Editor M. Andersen. *(Corresponding author: Xing Zhang.)*

Siwei Yang, Xing Zhang, Yuhua Hu, Mingda Wang, and Fusheng Wang are with the School of Electrical Engineering and Automation, Hefei University of Technology, Hefei 230009, China (e-mail: 2683130370@qq.com; honglf@ustc.edu.cn; hfut_hyh@163.com; wmd6094@mail.hfut.edu.cn; 10748451@qq.com).

Wang Mao is with the Shanghai Institute of Space Power-Sources, Shanghai 200245, China (e-mail: hfut_maow@163.com).

Renxian Cao is with the Sungrow Power Supply Co., Ltd., Hefei 230088, China (e-mail: crx@sungrow.cn).

Color versions of one or more of the figures in this article are available online at https://ieeexplore.ieee.org.

Digital Object Identifier 10.1109/TPEL.2020.3024282

[29] and [30] proposed the optimized third harmonic injection method, further extended the power routing range, and derived the distribution method of the positive third harmonic voltage. Similarly, discontinuous modulation makes the max modulation degree of some H-bridge reach 1.22 when the number of total H-bridge is three and output voltage of two H-bridges are clamped at either the positive or negative dc-link voltage at some time in a period [31]. Actually, the principle of discontinuous pulse width modulation (PWM) is similar with third harmonic injection, the difference between them is just injected waveform [32]–[34] Therefore, the detailed analysis will not be discussed below. The work in [35]–[40] proposed a hybrid pulse width modulation (HPWM) strategy combining low frequency square wave modulation and high frequency PWM. It can make some H-bridge units with large output power nearly realize the square wave modulation, thus, its modulation degree can reach 1.27. Therefore, the single-phase CHB PV grid-connected inverter can operate stably under a wider range of power routing conditions.

It mainly focuses on the improvement of the power routing control methods of the single-phase CHB PV grid-connected inverter in the existing researches, and there are few comparative analyses involving multiple power routing control methods. Moreover, the existing methods are only qualitative analyses and lack of scientific quantification means for the power routing range of single-phase CHB PV grid-connected inverter.

This article first introduces several typical power routing control methods of single-phase CHB PV grid-connected inverter based on fundamental voltage reconstruction, third harmonic injection, and HPWM. Second, the expressions of power routing ranges of different methods are derived. Finally, the power routing space (PRS) and power routing factor (PRF) proposed in [41] are adopted to qualitatively and quantitatively compare the power routing capabilities of various methods.

The rest of this article is organized as follows. Section II introduces three typical power routing control methods of single-phase CHB PV grid-connected inverter based on fundamental voltage reconstruction, derives the expressions of power routing ranges, and compares the power routing capabilities of three methods quantitatively. Sections III and IV introduce power routing control methods based on third harmonic injection and HPWM, respectively, and compare their power routing capabilities in detail. In Sections V, simulation results are presented to verify the validity of the theoretical analyses. Finally, Section VI concludes this article.

## II. Power Routing Control Method Based on Fundamental Voltage Reconstruction

The block diagram of a single-phase CHB PV grid-connected inverter is depicted in Fig. 1. It consists of $n$ H-bridge units and each H-bridge unit is connected to a PV module on the dc-side. Due to factors such as different light intensity, temperature, or different aging degree of PV modules, the output power of some PV modules is relatively large, while others are relatively small. When the PV module is operating at its maximum power point,

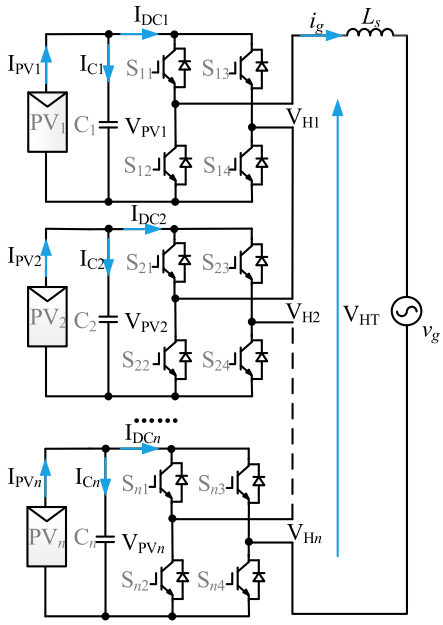


Fig. 1. Block diagram of single-phase CHB PV grid-connected inverter.

the corresponding dc-side voltage of each H-bridge unit will drift due to uneven power distribution.

The fundamental voltage reconstruction can be used to mitigate the problem of power imbalance, which means that the active component of the output voltage of each H-bridge unit is distributed in proportion to its dc-side input power. This control method can be divided into three types according to the reactive power allocation of the H-bridge unit, which are: system reactive power distributed by each H-bridge unit according to input power; system reactive power undertaken by specific H-bridge unit; system reactive power shared by each H-bridge unit equally.

### A. System Reactive Power Distributed by Each H-Bridge Unit According to Its Input Power

Alonso *et al.* [16] and Negroni *et al.* [17] proposed a power routing control method suitable for single-phase CHB PV grid-connected inverters, and its control block diagram is shown in Fig. 2. The entire control system includes three parts: dc-side voltage control, grid-side current control, and total modulation wave distribution. First, the dc-side output current reference value $I_{dc\,i}(i = 1, 2, \ldots, n)$ of the H-bridge unit is obtained through the dc-side voltage control. Then, the H-bridge unit output power $P_i$ and the total inverter output power $P_T$ are calculated, and the entire inverter output voltage $V_{HT}$ can be obtained by performing the closed-loop control on the $P_T$. Finally, the carrier phase shift-sinusoidal pulsewidth modulation (CPS-SPWM) is used to obtain the switching signals of each H-bridge unit.

Based on the abovementioned control methods, Kouro *et al.* [18], Chavarria *et al.* [19], and Huang *et al.* [20] changed the dc-side voltage control and grid-side current control. Its control block diagram is depicted in Fig. 3. There are two voltage control loops in the control method. A total voltage

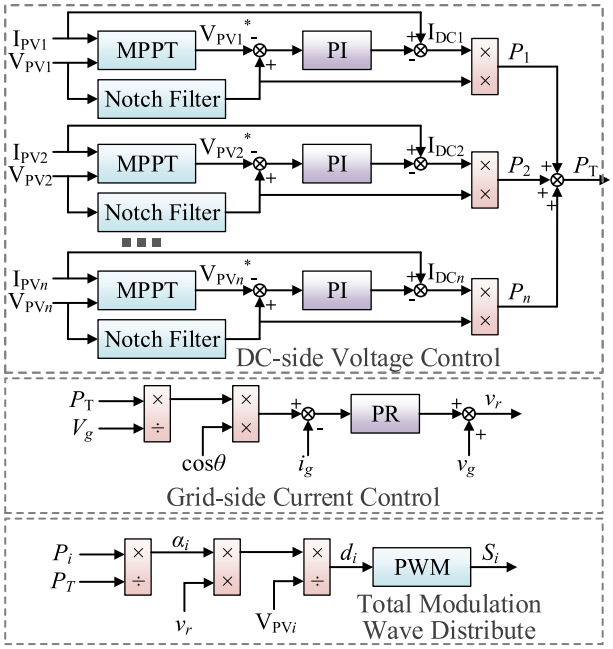


Fig. 2. Power routing control block diagram I based on fundamental voltage reconstruction.

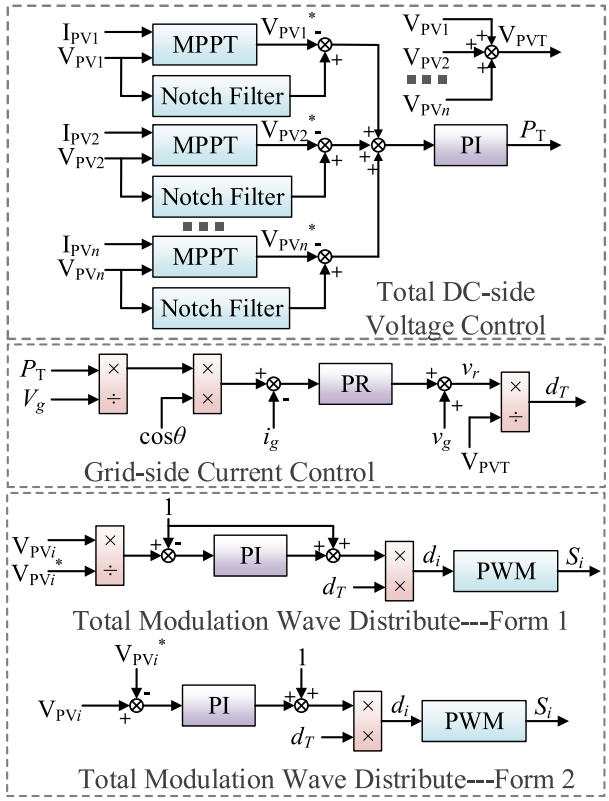


Fig. 3. Power routing control block diagram II based on fundamental voltage reconstruction.

loop ensures the overall dc-side voltage stability of the system through PI controller, and the voltage loops of the $n$ H-bridge units are used to adjust each dc-side voltage. The method of this adjustment is realized by feed-forward compensation for the modulation wave of each H-bridge unit in the modulation process. As can be seen from Fig. 3, there are two forms of feed-forward compensation. One is to adjust the per unit dc-side voltage deviation (($V_{PVi}/V_{PVi}^*$)-1), and the other is to directly adjust the dc-side voltage deviation ($V_{PVi}$-$V_{PVi}^*$). The two methods shown in Figs. 2 and 3 are essentially the same, they are both gained by multiplying the distribution coefficient obtained by the dc-side voltage change of each H-bridge unit with the total output voltage modulation wave of the inverter. These two methods directly modify the modulation ratio of the corresponding H-bridge unit in order to make each PV module operates at its maximum power point.

Fig. 4 shows a vector diagram of a three-unit CHB PV grid-connected inverter when this type of control method is used. Orienting the grid voltage vector $\boldsymbol{V_g}$ as the $d$-axis, the direction perpendicular to the $d$-axis is recorded as the $q$-axis, and $\boldsymbol{I_g}$ is the grid current vector; $\boldsymbol{V_i}$ is the fundamental voltage vector of the $i$th H-bridge unit; $\boldsymbol{V_L}$ is the filtered inductor voltage vector; $\boldsymbol{V_r}$ is the vector of fundamental voltage output by inverter; $\boldsymbol{V_{id}}$ and $\boldsymbol{V_{iq}}$ are the sum of the active voltage vectors and reactive voltage vectors of $\boldsymbol{V_i}$ on the $d$-axis and $q$-axis, respectively.

From Fig. 4, (1) could be obtained

$$\begin{cases} \mathbf{V_r} = \mathbf{V_g} + j\omega L_s \mathbf{I_g} = \mathbf{V_1} + \mathbf{V_2} + \mathbf{V_3} \\ \mathbf{V_1} = \mathbf{V_{1d}} + \mathbf{V_{1q}} = (d_1 + jq_1)\,\mathrm{V}_{PV1} \\ \mathbf{V_2} = \mathbf{V_{2d}} + \mathbf{V_{2q}} = (d_2 + jq_2)\,\mathrm{V}_{PV2} \\ \mathbf{V_3} = \mathbf{V_{3d}} + \mathbf{V_{3q}} = (d_3 + jq_3)\,\mathrm{V}_{PV3} \end{cases} \tag{1}$$

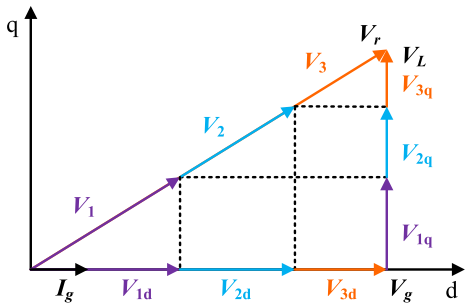


Fig. 4. Phasor diagram of the first type power routing control method.

where $d_i$ and $q_i$ are the active component and reactive component of the duty cycle of each H-bridge unit, respectively.

Since the light intensity has little effect on the voltage at the maximum power point, in order to simplify the analysis, it is assumed here that the dc-side voltage of each H-bridge unit is approximately equal, and recorded as $\mathrm{V_{dc}}$. Then, (1) could be rewritten as

$$\begin{cases} d_1 + d_2 + d_3 = \dfrac{\sqrt{2}V_g}{\mathrm{V_{dc}}} \\ q_1 + q_2 + q_3 = \dfrac{\sqrt{2}\omega L_s I_g}{\mathrm{V_{dc}}}. \end{cases} \tag{2}$$

Ignoring the inverter loss, the total output power $P_T$ of PV modules is equal to the ac output power of the inverter, and

the root-mean-square value of the grid current $I_g$ can be expressed as

$$I_g = \frac{P_T}{V_g} = \frac{P_1 + P_2 + P_3}{V_g}. \tag{3}$$

The active power output by each H-bridge unit is equal to the power output by its PV module, i.e.,

$$P_i = \frac{d_i \mathrm{V_{dc}} I_g}{\sqrt{2}}. \tag{4}$$

From (3) and (4), the active component of the duty cycle of each H-bridge unit can be obtained as

$$d_i = \sqrt{2}\frac{P_i V_g}{P_T \mathrm{V_{dc}}}. \tag{5}$$

It can be seen from the vector diagram that the reactive power of the system is distributed in proportion to the input power of each H-bridge unit, i.e.,

$$\frac{Q_i}{Q_T} = \frac{q_i \mathrm{V_{dc}}}{\sqrt{2}\omega L_s I_g} = \frac{P_i}{P_T}. \tag{6}$$

From (6), the reactive component of duty cycle of each H-bridge unit can be obtained as

$$q_i = \frac{\sqrt{2}\omega L_s P_i}{\mathrm{V_{dc}} V_g}. \tag{7}$$

To avoid overmodulation when the system operates stably, it needs to meet

$$\sqrt{d_i^2 + q_i^2} \le 1. \tag{8}$$

Substituting (7) into (8), it can be derived as

$$d_i \le \sqrt{1 - q_i^2} = \sqrt{1 - \left(\frac{\sqrt{2}\omega L_s P_i}{\mathrm{V_{dc}} V_g}\right)^2}. \tag{9}$$

Combining (5) and (9), it could be derived as

$$\frac{P_i}{P_T} \le \frac{\mathrm{V_{dc}}}{\sqrt{2} V_g}\sqrt{1 - \left(\frac{\sqrt{2}\omega L_s P_i}{\mathrm{V_{dc}} V_g}\right)^2}. \tag{10}$$

### *B. System Reactive Power Undertaken by Specific H-Bridge Unit*

Dell'Aquila *et al.* [21], Villanueva *et al.* [22], and Liu *et al.* [23] proposed a new power routing control method, and its control block diagram is shown in Fig. 5. The entire control system includes $n$+1 control loops, where $n$ dc-side voltage loops are responsible for maintaining the stability of the dc-side voltage of each H-bridge unit, and the current loop is responsible for achieving unit power factor operation. The characteristic of this type of control method is that the reactive power of the system is all provided by the first H-bridge unit, and the remaining H-bridge units only output active power. In essence, this method controls the amplitude and phase of the modulation voltage of the first H-bridge unit, then the phases of the modulation voltage of the remaining $n$-1 H-bridge units are consistent with

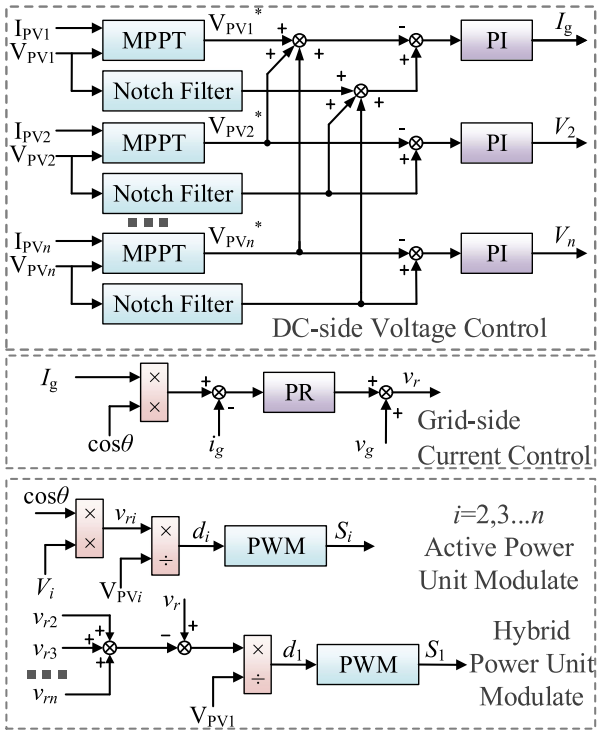


Fig. 5. Power routing control block diagram III based on fundamental voltage reconstruction.

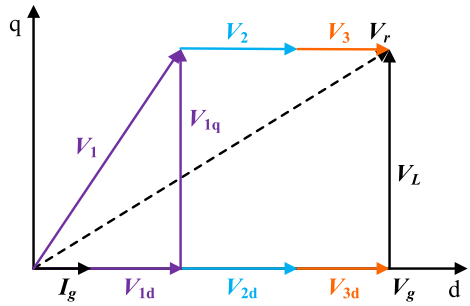


Fig. 6. Phasor diagram of the second type power routing control method.

the grid voltage, at the same time only corresponding amplitude is changed to achieve its MPPT.

Fig. 6 shows a vector diagram of a three-unit CHB PV grid-connected inverter controlled by this type of control method. The duty cycle active component of each H-bridge unit is the same as the first type of power routing control method, so no more detail description here. The duty cycle reactive component of each H-bridge unit can be calculated as

$$\begin{cases} q_1 = \dfrac{\sqrt{2}\omega L_s I_g}{\mathrm{V_{dc}}} \\ q_2 = q_3 = 0. \end{cases} \tag{11}$$

To avoid overmodulation when the system operates stably, it needs to meet

$$\begin{cases} d_1 \le \sqrt{1 - q_1^2} = \sqrt{1 - \left(\frac{\sqrt{2}\omega L_s I_g}{\mathrm{V_{dc}}}\right)^2} \\ d_i \le 1 i = 2, 3 \ldots n. \end{cases} \tag{12}$$

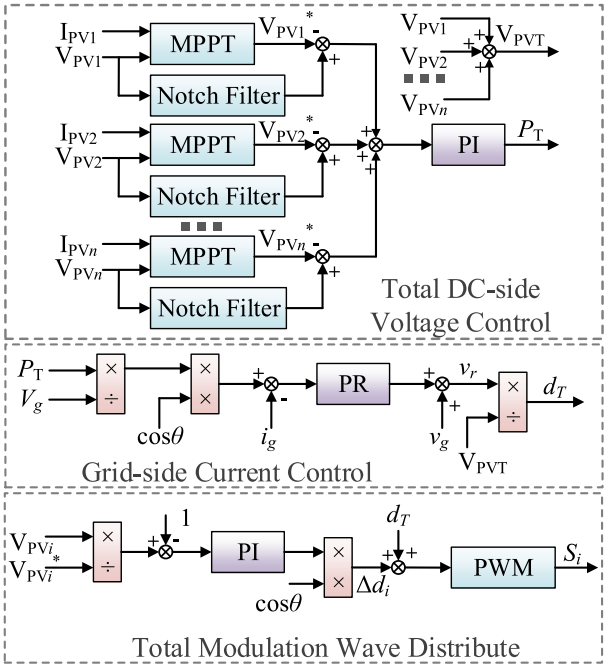


Fig. 7. Power routing control block diagram IV based on fundamental voltage reconstruction.

Substituting (5) into (12), it could be obtained as

$$\begin{cases} \frac{P_1}{P_T} \le \frac{\mathrm{V_{dc}}}{\sqrt{2}V_g}\sqrt{1-\left(\frac{\sqrt{2}\omega L_s I_g}{\mathrm{V_{dc}}}\right)^2} \\ \frac{P_i}{P_T} \le \frac{\mathrm{V_{dc}}}{\sqrt{2}V_g} i = 2,3\ldots n. \end{cases} \tag{13}$$

### C. System Reactive Power Shared by Each H-Bridge Unit Equally

Zhao *et al.* [24] and Wang *et al.* [26] proposed a power routing control method based on the active component modification of duty cycle. The control block diagram of this method is depicted in Fig. 7. The entire control system includes three parts: total dc-side voltage control, grid-side current control, and power routing control. The principle of power routing control is: the modified duty cycle signal $\Delta d_i$ is gained by multiplying the grid voltage synchronization factor with the value obtained by the per unit dc-side deviation of each H-bridge unit after PI controller. And then the modified duty cycle $\Delta d_i$ is superimposed on the total duty cycle signal $d_T$ output by the grid current loop to form the final duty cycle signal of each H-bridge unit for CPS-SPWM. The characteristic of this type of control method is that each H-bridge unit shares the reactive power of the system equally.

Fig. 8 shows a vector diagram of a three-unit CHB PV grid-connected inverter when this type of control method is used. The active component of the duty cycle of each H-bridge unit is the same as the first type of power routing control method. The duty cycle reactive component of each H-bridge unit is

$$q_i = \frac{\sqrt{2}\omega L_s I_g}{n\mathrm{V_{dc}}}. \tag{14}$$

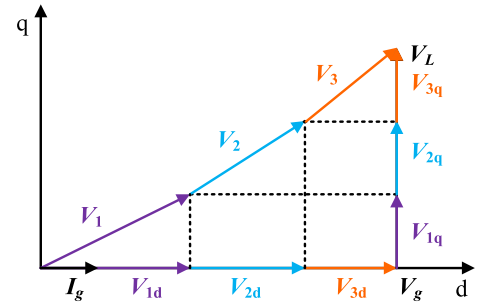


Fig. 8. Phasor diagram of the third type power routing control method.

To avoid overmodulation when the system operates stably, it needs to meet

$$d_i \le \sqrt{1-q_i^2} = \sqrt{1-\left(\frac{\sqrt{2}\omega L_s P_g}{n\mathrm{V_{dc}}V_g}\right)^2}. \tag{15}$$

Substituting (5) into (15), it could be derived as

$$\frac{P_i}{P_T} \le \frac{\mathrm{V_{dc}}}{\sqrt{2}V_g}\sqrt{1-\left(\frac{\sqrt{2}\omega L_s P_T}{n\mathrm{V_{dc}}V_g}\right)^2}. \tag{16}$$

In order to make the analysis more general, the power imbalance coefficient $\lambda_i (i = 1,2,\ldots,n)$ of the H-bridge unit is defined as

$$\lambda_i = \frac{nP_i}{P_N} \tag{17}$$

where $P_N$ is the rated output power of the system.

Define the per unit value of filter inductor $L^*$ as

$$L^* = L_s \Big/ \frac{V_g^2}{2\pi f P_N} = \frac{2\pi f L_s P_N}{V_g^2}. \tag{18}$$

Define the voltage overrating $\xi$ as

$$\xi = \frac{n\mathrm{V_{dc}}}{\sqrt{2}V_g\sqrt{1+(L^*)^2}} - 1. \tag{19}$$

Substituting (17)–(19) into (10), the constraint of the first type of power routing control method could be derived as

$$\frac{\lambda_i}{\sum_{i=1}^n \lambda_i} \le \frac{(1+\xi)\sqrt{1+(L^*)^2}}{n}\sqrt{1-\left(\frac{\lambda_i L^*}{(1+\xi)\sqrt{1+(L^*)^2}}\right)^2}. \tag{20}$$

Substituting (17)–(19) into (13), the constraints of the second type of power routing control method could be obtained as

$$\begin{cases} \frac{\lambda_1}{\sum_{i=1}^n \lambda_i} \le \frac{(1+\xi)\sqrt{1+(L^*)^2}}{n}\sqrt{1-\left(\frac{L^*\sum_{i=1}^n \lambda_i}{(1+\xi)\sqrt{1+(L^*)^2}}\right)^2} \\ \frac{\lambda_i}{\sum_{i=1}^n \lambda_i} \le \frac{(1+\xi)\sqrt{1+(L^*)^2}}{n} i = 2,3\ldots n. \end{cases} \tag{21}$$

Similarly, substituting (17)–(19) into (16), the constraint of the third type of power routing control method could be derived

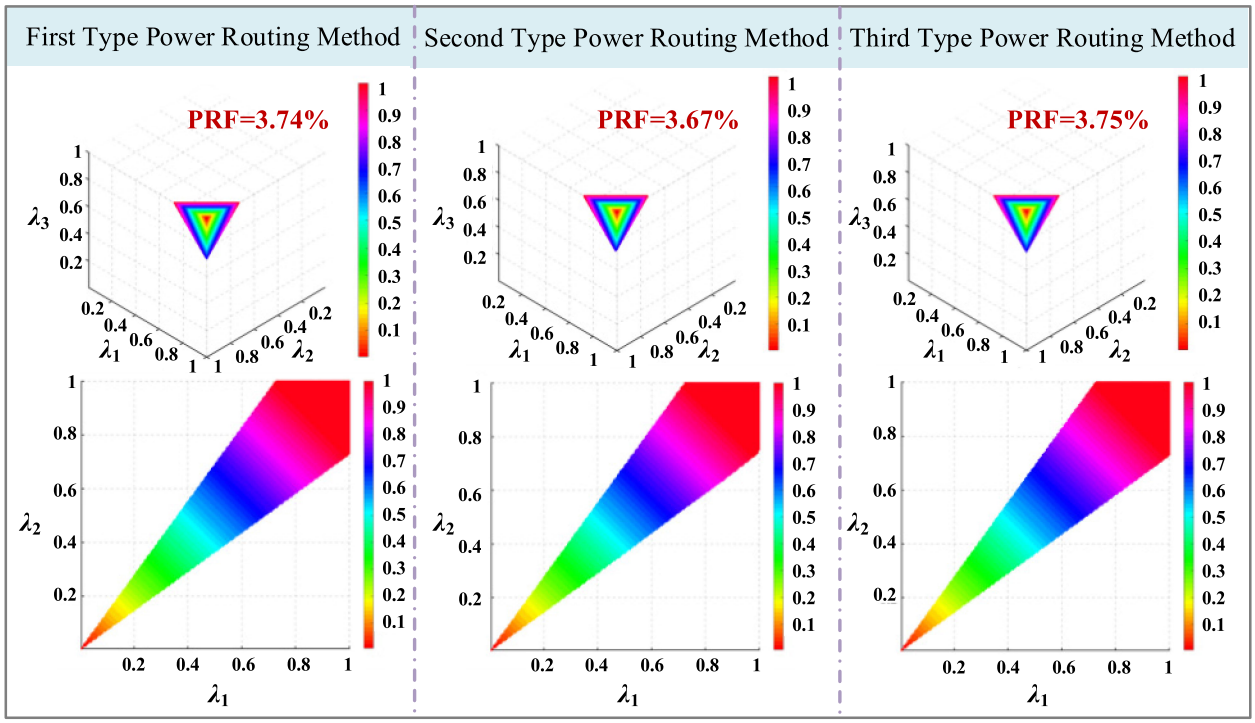


Fig. 9. Routing range of three kinds of power routing control methods with $L^* = 5\%$ and $\xi = 10\%$.

as

$$\frac{\lambda_i}{\sum_{i=1}^{n}\lambda_i} \le \frac{(1+\xi)\sqrt{1+(L^*)^2}}{n} \times \sqrt{1-\left(\frac{L^*\sum_{i=1}^{n}\lambda_i}{n(1+\xi)\sqrt{1+(L^*)^2}}\right)^2}. \quad (22)$$

In order to compare the power routing capabilities of various power routing control methods more intuitively, the qualitative and quantitative analyses are given in this article. The qualitative index is PRS, that is, multidimensional space graph is utilized to describe the power routing range. The quantitative index is PRF, which directly reflects the percentage of viable cases that can be rebalanced among all possible power imbalance cases. Taking $n$-unit CHB PV grid-connected inverter as an example, an $n$-dimensional space with the form of $1*1\ldots*1$ can be established by the power imbalance coefficient ($\lambda_1$, $\lambda_2$, …, $\lambda_n$) of each H-bridge unit. Each power imbalance case can be represented by a unique operation point ($\lambda_1'$, $\lambda_2'$, …, $\lambda_n'$) in the space. If the maximum output voltage of each H-bridge unit is lower than its available dc-side voltage

$$\max\{v_{r1}, v_{r2}, \ldots, v_{rn}\}(\lambda_1, \lambda_2, \ldots, \lambda_n) \le \mathrm{V_{dc}}. \quad (23)$$

Then, the grid current with low harmonic distortion can be generated without overmodulation of H-bridge unit and this operation point can be rebalanced using a given method. All operation points that can be rebalanced form an $n$-dimensional space, defined as the PRS. The volume of the PRS is defined as the PRF

$$\mathrm{PRF} = \int_0^1 \int_0^1 \cdots \int_0^1 F(\lambda_1, \lambda_2, \ldots \lambda_n) d\lambda_1 d\lambda_2 \ldots d\lambda_n \quad (24)$$

where

$$F(\lambda_1, \lambda_2, \ldots \lambda_n) = \begin{cases} 1, & \max\{v_{r1}, v_{r2}, \ldots, v_{rn}\}(\lambda_1, \lambda_2, \ldots, \lambda_n) \le \mathrm{V_{dc}} \\ 0, & \max\{v_{r1}, v_{r2}, \ldots, v_{rn}\}(\lambda_1, \lambda_2, \ldots, \lambda_n) > \mathrm{V_{dc}}. \end{cases} \quad (25)$$

It can be seen from (20)–(22) that the power routing ranges of these three methods are related to the per unit filter inductor $L^*$, the number of H-bridge unit $n$ and the voltage overrating $\xi$. It is difficult to draw its power routing range when the number of H-bridge units is larger than three. Therefore, only the power routing range of the three-unit CHB PV grid-connected inverter is given here. Fig. 9 shows the PRSs of three types of power routing control methods and their PRFs when $L^* = 5\%$ and $\xi = 10\%$. It can be seen from the figure that the PRSs of the three types of methods are only slightly different, and their PRFs are 3.74%, 3.67%, and 3.75%, respectively. Under the same conditions, the third type of control method has the largest power routing capability, followed by the first type of control method, and finally the second type of control method.

Figs. 10 and 11 show the relationship between the PRFs of three types of power routing control methods and the per unit value of filter inductor $L^*$ and the voltage overrating $\xi$. As can be seen from Fig. 10, as the parameter $L^*$ becomes larger, the PRFs of the first and third methods gradually increases, while

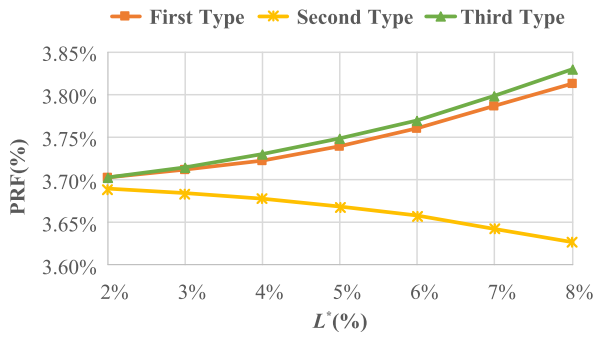


Fig. 10. PRF of three kinds of power routing control methods under $\xi = 10\%$ and different $L^*$ parameters.

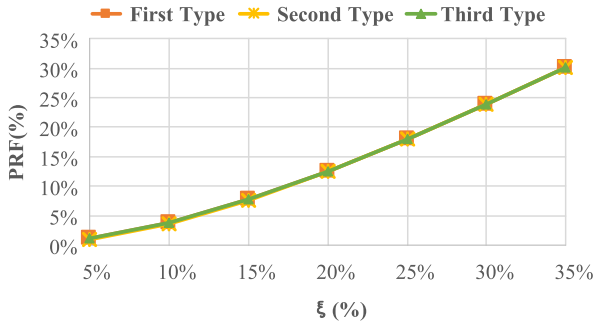


Fig. 11. PRF of three kinds of power routing control methods under $L^* = 5\%$ and different $\xi$ parameters.

the PRF of the second method gradually decreases. But on the whole, PRFs of the three methods have little change. Therefore, the value of the filter inductor has little effect on the PRS. In Fig. 11, as the parameter $\xi$ becomes larger, the PRFs of all three methods increase significantly. The three curves are basically consistent, because the difference between PRFs of the three methods is very small. The larger the parameter $\xi$, the larger the corresponding dc-side voltage, and the less likely the system is to saturate.

## III. Power Routing Control Method by Third Harmonic Injection

According to the analysis in the previous section, although the power routing control method based on fundamental voltage reconstruction can realize unequal power distribution between H-bridges, its power routing range is small. On this basis, Ko *et al.* [28] proposed a method of third harmonic injection, so that the modulation degree of some H-bridge units with high output power reached 1.155, which improved the utilization rate of the dc-side voltage, thereby expanding the power routing range of CHB grid-connected inverters. As shown in Fig. 12, a three-unit CHB PV grid-connected inverter is taken as an example. The principle of this control method is to inject the negative third harmonic of 1/6 times the amplitude into the two overmodulated H-bridge units to avoid overmodulation, and to inject the positive third harmonic into the normal H-bridge unit. Therefore, how to allocate the positive third harmonic is a key issue, but it is not mentioned in the literature [28]. Based on [28]–[30] further proposed an optimized third harmonic injection method. On the one hand, it is pointed out that although the negative third harmonic with a fixed injection of 1/6 times the amplitude can improve the dc-side voltage utilization of the overmodulated unit to 1.155, it may cause the risk of overmodulation of the normal unit; On the other hand, a specific positive third harmonic distribution scheme is proposed. In order to describe the difference between the two methods more clearly, the modulation voltage $v_r^*$ after the third harmonic injection is defined as

$$v_r^* = m_1 \cos(\omega t) + m_1 m_3 \cos(3\omega t) \tag{26}$$

where $m_1$ is the modulation degree of the fundamental modulation voltage, $m_3$ is the third harmonic compensation coefficient, and $\omega t$ is the phase angle of the fundamental modulation voltage.

Assuming $m_1$ is 1, the relationship between $\omega t$, $m_3$, and $v_r^*$ is shown in Fig. 13(a), and its y-z view is shown in Fig. 13(b). As the figure depicted that the maximum value of the modulation voltage $v_r^*$ decreases first and then increases with the increase of $m_3$. When $m_3 = -1/6$, its value reaches the minimum. When $m_3 = -1/6$, max $(v_r{}^*) = 0.866$, which makes the linear modulation range of the modulation voltage up to about 1.155. It can be further seen from Fig. 13(b) that when $-0.408 \leq m_3 \leq 0$, no overmodulation occurs, i.e., the shaded area in the figure. That is to say, in this case, the negative third harmonic with a maximum amplitude of 0.408 times can be injected, the negative third harmonic with a magnitude of 1/6 times can also be injected and of course neither the negative third harmonic has to be injected. However, the total third harmonic voltage in a single-phase system needs to be zero. Therefore, a certain amplitude of negative third harmonic is injected into the system, correspondingly, the same amplitude of positive third harmonic needs to be injected. As can also be seen from the figure that the larger the amplitude of the positive third harmonic injected, the larger the amplitude of the modulation voltage, and the greater the risk of overmodulation. Zhao *et al.* [29] proposed to compensate the modulation amplitude of the H-bridge unit to 1, so as to inject the least amount of negative third harmonic into the system. The normal unit reduces the risk of overmodulation by injecting a minimum amount of positive third harmonics.

Fig. 14 shows the relationship between the third harmonic compensation coefficient $m_3$ of the overmodulation unit and the fundamental modulation degree $m_1$, when two kinds of third harmonic injection methods are utilized. It is clear that the two methods are different, one is to always maintain the third harmonic compensation coefficient $m_3 = -1/6$, i.e., the negative third harmonic is injected with the maximum amplitude; The other is to gradually increase the negative third harmonic injection as the fundamental modulation degree $m_1$ increases.

The traditional third harmonic injection method is used as an example to derive the power routing range. The amplitude $V_{\mathrm{r}}$ of the fundamental component of the ac output voltage of the inverter can be expressed as

$$V_r = \sqrt{2}\sqrt{(V_g)^2 + \left(2\pi f L_s \frac{P_T}{V_g}\right)^2}. \tag{27}$$

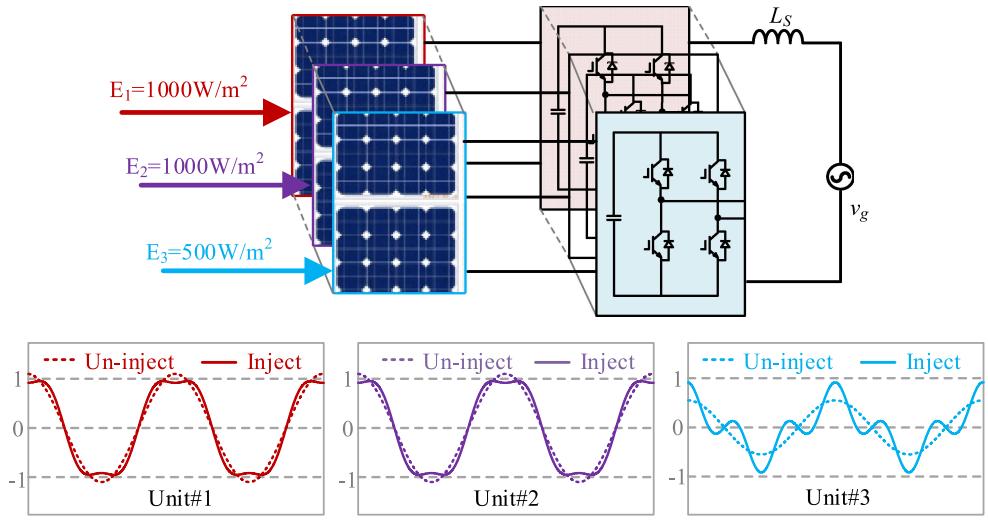


Fig. 12. Principle of power routing control method based on third harmonic injection.

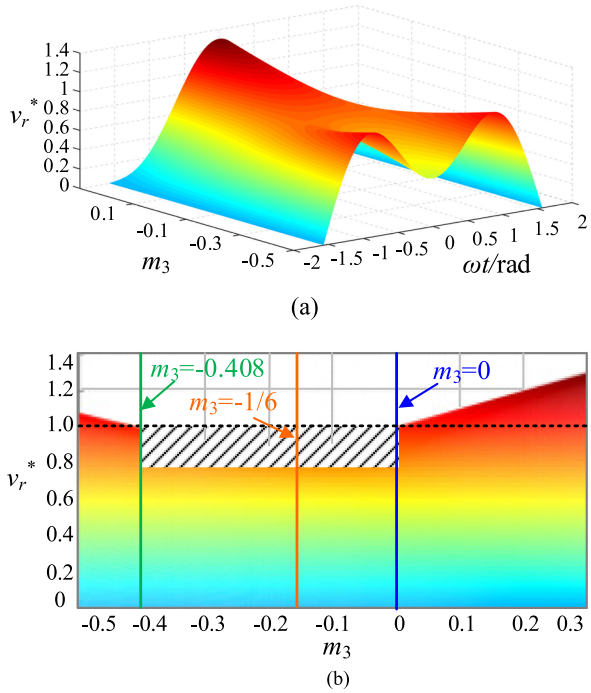


Fig. 13. Relationship curve of $\omega t$, $m_3$, and $v_r^*$. (a) Three-dimensions view. (b) y–z view.

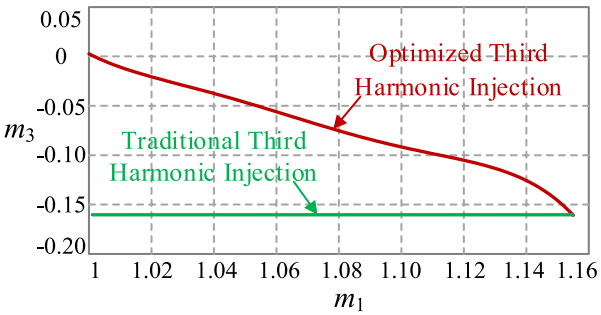


Fig. 14. Relationship curve of $m_1$ and $m_3$.

Substituting (17) and (18) into (27), it could be obtained as

$$V_r = \sqrt{2}V_g\sqrt{1+\left(\frac{1}{n}\sum\nolimits_{i=1}^{n}\lambda_i\frac{2\pi f L_s P_N}{V_g^2}\right)^2} = \sqrt{2}V_g\sqrt{1+\left(\frac{1}{n}\sum\nolimits_{i=1}^{n}\lambda_i L^*\right)^2}. \tag{28}$$

The phase $\varphi$ of the fundamental component of the ac output voltage of the inverter could be expressed as

$$\varphi = \arctan\left(\frac{2\pi f L_s \frac{1}{n}\sum_{i=1}^{n}\lambda_i P_N}{V_g^2}\right) = \arctan\left(\frac{1}{n}\sum_{i=1}^{n}\lambda_i L^*\right). \tag{29}$$

The fundamental component $v_r$ of the ac output voltage of the inverter could be obtained as

$$v_r = \sqrt{2}V_g\sqrt{1+\left(\frac{1}{n}\sum\nolimits_{i=1}^{n}\lambda_i L^*\right)^2}\cos\left(\omega t+\arctan\left(\frac{1}{n}\sum_{i=1}^{n}\lambda_i L^*\right)\right). \tag{30}$$

Before the third harmonic is injected, the fundamental component $v_{ri}$ of the ac output voltage of each H-bridge unit could be expressed as

$$v_{ri} = \frac{P_i}{P_T}v_r = \frac{\lambda_i}{\sum_{i=1}^{n}\lambda_i}\sqrt{2}V_g\sqrt{1+\left(\frac{1}{n}\sum\nolimits_{i=1}^{n}\lambda_i L^*\right)^2}\cos\left(\omega t+\arctan\left(\frac{1}{n}\sum_{i=1}^{n}\lambda_i L^*\right)\right). \tag{31}$$

Then, the modulation degree $m_i$ of the fundamental wave of each H-bridge unit could be derived as

$$m_i = \frac{\lambda_i}{\sum_{i=1}^{n}\lambda_i}\sqrt{2}V_g\sqrt{1+\left(\frac{1}{n}\sum\nolimits_{i=1}^{n}\lambda_i L^*\right)^2}/\mathrm{V_{dc}}. \quad (32)$$

Substituting (19) into (29), it could be obtained as

$$m_i = \frac{n\lambda_i\sqrt{1+\left(\frac{1}{n}\sum_{i=1}^{n}\lambda_i L^*\right)^2}}{(1+\xi)\sqrt{1+(L^*)^2}\sum_{i=1}^{n}\lambda_i}. \quad (33)$$

Assuming that $l\,(1\le l<n)$ H-bridge units are overmodulated. When the traditional third harmonic injection is used, the ac output voltage of each H-bridge unit is

$$\begin{cases} v_{\mathrm{NT}k} = \frac{\lambda_k}{\sum_{i=1}^{n}\lambda_i}\sqrt{2}V_g\sqrt{1+\left(\frac{1}{n}\sum_{i=1}^{n}\lambda_i L^*\right)^2} \\ \quad \cos\left(\omega t+\arctan\left(\frac{1}{n}\sum_{i=1}^{n}\lambda_i L^*\right)\right) \\ \quad -\frac{1}{6}m_k\mathrm{V_{dc}}\cos\left(3\omega t+3\arctan\left(\frac{1}{n}\sum_{i=1}^{n}\lambda_i L^*\right)\right) \\ i=1,2,\ldots,n,k=1,2,\ldots,l \\ v_{\mathrm{PT}j} = \frac{\lambda_j}{\sum_{i=1}^{n}\lambda_i}\sqrt{2}V_g\sqrt{1+\left(\frac{1}{n}\sum_{i=1}^{n}\lambda_i L^*\right)^2} \\ \quad \cos\left(\omega t+\arctan\left(\frac{1}{n}\sum_{i=1}^{n}\lambda_i L^*\right)\right)+\frac{1}{6}W_j\sum_{k=1}^{l}m_k\mathrm{V_{dc}} \\ \quad \cos\left(3\omega t+3\arctan\left(\frac{1}{n}\sum_{i=1}^{n}\lambda_i L^*\right)\right) \\ i=1,2,\ldots,n,j=l+1,l+2,\ldots,n \end{cases} \quad (34)$$

where $v_{\mathrm{NT}k}$ is the ac output voltage of the overmodulated unit, and $v_{\mathrm{PT}j}$ is the ac output voltage of the normal unit, $W_{\mathrm{j}}$ is the distribution coefficient of the positive third harmonic, and its expression is

$$W_j = \frac{1-m_j}{\sum_{j=l+1}^{n}(1-m_j)} = \frac{(1+\xi)\sqrt{1+(L^*)^2}\sum_{i=1}^{n}\lambda_i - n\lambda_j\sqrt{1+\left(\frac{1}{n}\sum_{i=1}^{n}\lambda_i L^*\right)^2}}{\sum_{j=l+1}^{n}\left((1+\xi)\sqrt{1+(L^*)^2}\sum_{i=1}^{n}\lambda_i - n\lambda_j\sqrt{1+\left(\frac{1}{n}\sum_{i=1}^{n}\lambda_i L^*\right)^2}\right)}. \quad (35)$$

Substituting (33) into (34), $v_{\mathrm{NT}k}$ could be obtained as

$$v_{\mathrm{NT}k} = \frac{\lambda_k}{\sum_{i=1}^{n}\lambda_i}\sqrt{2}V_g\sqrt{1+\left(\frac{1}{n}\sum\nolimits_{i=1}^{n}\lambda_i L^*\right)^2}\cos\left(\omega t+\arctan\left(\frac{1}{n}\sum_{i=1}^{n}\lambda_i L^*\right)\right) - \frac{\sqrt{2}}{6}\frac{\lambda_k V_g}{\sum_{i=1}^{n}\lambda_i}\sqrt{1+\left(\frac{1}{n}\sum\nolimits_{i=1}^{n}\lambda_i L^*\right)^2}\cos\left(3\omega t+3\arctan\left(\frac{1}{n}\sum_{i=1}^{n}\lambda_i L^*\right)\right) \quad i=1,2,\ldots,n,k=1,2,\ldots,l. \quad (36)$$

Substituting (33) and (35) into (34), $v_{\mathrm{PT}j}$ could be obtained as

$$v_{\mathrm{PT}j} = \frac{\lambda_j}{\sum_{i=1}^{n}\lambda_i}\sqrt{2}V_g\sqrt{1+\left(\frac{1}{n}\sum\nolimits_{i=1}^{n}\lambda_i L^*\right)^2}\cos\left(\omega t+\arctan\left(\frac{1}{n}\sum_{i=1}^{n}\lambda_i L^*\right)\right) + \frac{\sqrt{2}}{6}\frac{W_j V_g}{\sum_{i=1}^{n}\lambda_i}\sum_{k=1}^{l}\lambda_k\sqrt{1+\left(\frac{1}{n}\sum\nolimits_{i=1}^{n}\lambda_i L^*\right)^2}\cos\left(3\omega t+3\arctan\left(\frac{1}{n}\sum_{i=1}^{n}\lambda_i L^*\right)\right) \quad i=1,2,\ldots,n,k=1,2,\ldots,l,j=l+1,l+2,\ldots,n. \quad (37)$$

To avoid overmodulation when the system operates stably, it needs to meet

$$\begin{cases} v_{\mathrm{NT}k}\le \mathrm{V_{dc}}, k=1,2,\ldots,l \\ v_{\mathrm{PT}j}\le \mathrm{V_{dc}}, j=l+1,l+2,\ldots,n. \end{cases} \quad (38)$$

Substituting (19) into (38), it could be derived as

$$\begin{cases} \max\left(v_{\mathrm{NT}k}\right)\le \frac{\sqrt{2}(1+\xi)\sqrt{1+(L^*)^2}}{n}V_g \\ k=1,2,\ldots,l \\ \max\left(v_{\mathrm{PT}j}\right)\le \frac{\sqrt{2}(1+\xi)\sqrt{1+(L^*)^2}}{n}V_g \\ j=l+1,l+2,\ldots,n. \end{cases} \quad (39)$$

Substituting (36) and (37) into (39), the expression of power routing range could be obtained, as shown in (40) at the bottom of this page.

$$\max\left\{\begin{array}{c} \frac{\lambda_k}{\sum_{i=1}^{n}\lambda_i}\sqrt{1+\left(\frac{1}{n}\sum_{i=1}^{n}\lambda_i L^*\right)^2}\cos\left(\omega t+\arctan\left(\frac{1}{n}\sum_{i=1}^{n}\lambda_i L^*\right)\right) \\ -\frac{\lambda_k}{6\sum_{i=1}^{n}\lambda_i}\sqrt{1+\left(\frac{1}{n}\sum_{i=1}^{n}\lambda_i L^*\right)^2}\cos\left(3\omega t+3\arctan\left(\frac{1}{n}\sum_{i=1}^{n}\lambda_i L^*\right)\right) \\ \frac{\lambda_j}{\sum_{i=1}^{n}\lambda_i}\sqrt{1+\left(\frac{1}{n}\sum_{i=1}^{n}\lambda_i L^*\right)^2}\cos\left(\omega t+\arctan\left(\frac{1}{n}\sum_{i=1}^{n}\lambda_i L^*\right)\right) \\ +\frac{W_j}{6\sum_{i=1}^{n}\lambda_i}\sum_{k=1}^{l}\lambda_k\sqrt{1+\left(\frac{1}{n}\sum_{i=1}^{n}\lambda_i L^*\right)^2}\cos\left(3\omega t+3\arctan\left(\frac{1}{n}\sum_{i=1}^{n}\lambda_i L^*\right)\right) \\ i=1,2,\ldots,n,k=1,2,\ldots,l,j=l+1,l+2,\ldots,n \end{array}\right\} \le \frac{(1+\xi)\sqrt{1+(L^*)^2}}{n} \quad (40)$$

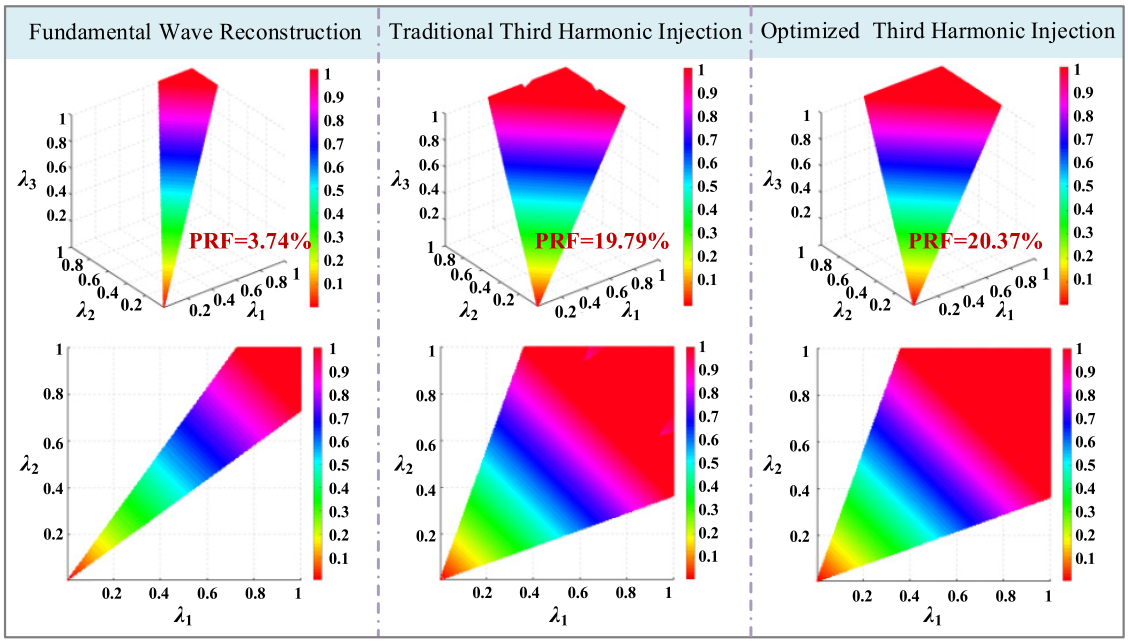


Fig. 15. Power routing range of power routing control methods based on third harmonic injection with $L^* = 5\%$ and $\xi = 10\%$.

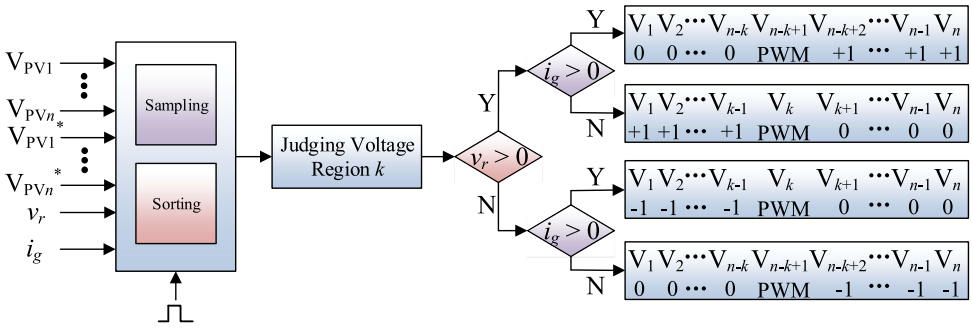


Fig. 16. Principle of HMSCZS.

The derivation of the power routing range of the optimized third harmonic injection method is the same as abovementioned, which will not be discussed here. Similarly, only the power routing range of the three-unit CHB PV grid-connected inverter is given here. Fig. 15 depicts the PRSs and PRFs of the two methods based on the third harmonic injection power routing control method when $L^* = 5\%$ and $\xi = 10\%$. As could be seen, compared with the method based on fundamental voltage reconstruction, the traditional third harmonic injection method significantly expands the PRS, and its PRF is 19.98%. The PRS based on the optimized third harmonic injection method is the largest, and its PRF is 20.37%. The effects of the parameters $L^*$ and $\xi$ on the system power routing range are consistent with the analysis in Section A, no more details here.

## IV. Power Routing Control Method Based on HPWM Modulation

In order to further expand the power routing range of CHB PV inverters, literature [35]–[40] proposed an HPWM modulation strategy combining low-frequency square-wave modulation and high-frequency PWM. The low-frequency square-wave modulation is used to realize the dc-side voltage balance of each H-bridge unit, and the high-frequency PWM improves the grid current quality. Because the maximum modulation degree of square wave is $4/\pi$, the modulation can effectively expand the power routing range of the system. HPWM can be divided into two types according to its switching mode allocation rules: hybrid modulation strategy containing zero state (HMSCZS) and hybrid modulation strategy without zero state. Because the principle of the two methods is similar, this article takes HMSCZS as an example to analyze.

As shown in Fig. 16, the main steps of HMSCZS are as follows.

1) Calculating the error between the actual value of dc-side voltage $V_{PVi}(i = 1,2,3 \ldots n)$ and its reference value $V_{PVi}^*$ $(i = 1,2,3 \ldots n)$ of each H-bridge unit

$$\Delta V_{PVi} = V_{PVi} - V_{PVi}^*. \tag{41}$$

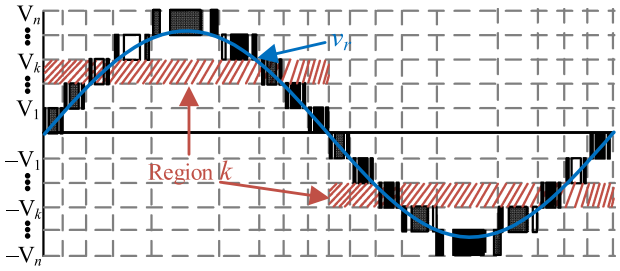


Fig. 17. Definition of $k$th voltage region.

2) Sorting the dc-side voltage error $\Delta V_{PVi}(i = 1, 2, 3 \ldots n)$ of each H-bridge unit in ascending order according to a certain frequency and mapping for the actual dc-side voltages derived from sorted vector of voltage errors ([$V_1$,$V_2$,…,$V_n$]).
3) The voltage region $k$ of the total modulation wave voltage $v_r$ is judged, according to formula (42), as shown in Fig. 17

$$\sum_{i=1}^{k-1} V_i < |v_r| < \sum_{i=1}^{k} V_i. \tag{42}$$

4) The switching modes of the $n$ H-bridge units are determined according to the polarity of the total modulation wave voltage $v_r$, the direction of the grid current $i_g$, and the voltage region $k$ where $v_r$ is located. For the convenience of description, the states "+1", "–1", "0" and PWM represent that the output voltages of H-bridge unit are $+V_{PVi}$, $-V_{PVi}$, 0 ,and PWM, respectively. The assignment rules of specific switching modes of each H-bridge unit are as following.
   a) If $v_r > 0, i_g > 0$: After sorting the dc-side voltages, the H-bridge units whose actual values of $V_j$ are $V_{n\text{-}k+2}$, $V_{n\text{-}k+3} \ldots V_n$, operate in the "+1" state, i.e., the discharge mode; the units whose actual values of $V_j$ are $V_1, V_2 \ldots V_{n\text{-}k}$, operate in the "0" state; the unit whose actual value of $V_j$ is $V_{n\text{-}k+1}$, operates in the PWM mode.
   b) If $v_r > 0$, $i_g \leq 0$: After sorting the dc-side voltages, the H-bridge units whose actual values of $V_j$ are $V_1$, $V_2 \ldots V_{k\text{-}1}$, operate in the "+1", state, i.e., the discharge mode; the units whose actual values of $V_j$ are $V_{k+1}$, $V_{k+2} \ldots V_n$, operate in the "0" state; the unit whose actual value of $V_j$ is $V_k$, operates in the PWM mode.
   c) If $v_r \leq 0$, $i_g > 0$: After sorting the dc-side voltages, the H-bridge units whose actual values of $V_j$ are $V_1$, $V_2 \ldots V_{k\text{-}1}$, operate in the "–1" state, i.e., the discharge mode; the units whose actual value of $V_j$ are $V_{k+1}$, $V_{k+2} \ldots V_n$, operate in the "0" state; the unit whose actual value of $V_j$ is $V_k$, operates in the PWM mode.
   d) If $v_r \leq 0, i_g \leq 0$: After sorting the dc-side voltages, the H-bridge units whose actual values of $V_j$ are $V_{n\text{-}k+2}$, $V_{n\text{-}k+3} \ldots V_n$, operate in the "–1" state, i.e., the discharge mode; the units whose actual value of $V_j$ are $V_, V_2 \ldots V_{n\text{-}k}$, operate in the "0" state; the unit whose actual value of $V_j$ is $V_{n\text{-}k+1}$, operates in the PWM mode.

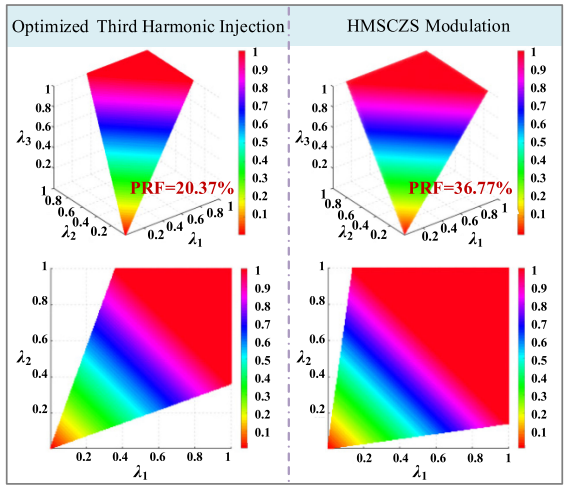


Fig. 18. Routing range of power routing control methods based on HPWM with $L^* = 5\%$ and $\xi = 10\%$.

The following uses the HMSCZS method as an example to derive its power routing range. From (30), it can be known that the fundamental component $v_r$ of the ac output voltage of the inverter could be expressed as

$$v_r = \sqrt{2}V_g\sqrt{1+\left(\frac{1}{n}\sum\nolimits_{i=1}^{n}\lambda_i L^*\right)^2} \cos\left(\omega t + \arctan\left(\frac{1}{n}\sum_{i=1}^{n}\lambda_i L^*\right)\right). \tag{43}$$

The fundamental component $v_{ri}$ of the ac-side output voltage of each H-bridge unit could be obtained as

$$v_{ri} = \frac{P_i}{P_T}v_r = \frac{\lambda_i}{\sum_{i=1}^{n}\lambda_i}\sqrt{2}V_g\sqrt{1+\left(\frac{1}{n}\sum\nolimits_{i=1}^{n}\lambda_i L^*\right)^2} \cos\left(\omega t + \arctan\left(\frac{1}{n}\sum_{i=1}^{n}\lambda_i L^*\right)\right). \tag{44}$$

In order to avoid overmodulation during the stable operation of the system, it is necessary to meet the following requirements:

$$\begin{cases} v_r \leq nV_{dc} \\ v_{ri} \leq \frac{4}{\pi}V_{dc}, i = 1, 2, \ldots, n. \end{cases} \tag{45}$$

Substituting (43) and (44) into (45), it could be obtained as

$$\begin{cases} \sqrt{2}V_g\sqrt{1+\left(\frac{1}{n}\sum_{i=1}^{n}\lambda_i L^*\right)^2} \\ \quad \cos\left(\omega t + \arctan\left(\frac{1}{n}\sum_{i=1}^{n}\lambda_i L^*\right)\right) \leq nV_{dc} \\ \frac{\lambda_i\sqrt{2}V_g}{\sum_{i=1}^{n}\lambda_i}\sqrt{1+\left(\frac{1}{n}\sum_{i=1}^{n}\lambda_i L^*\right)^2} \\ \quad \cos\left(\omega t + \arctan\left(\frac{1}{n}\sum_{i=1}^{n}\lambda_i L^*\right)\right) \leq \frac{4}{\pi}V_{dc} \\ i = 1, 2, \ldots, n. \end{cases} \tag{46}$$

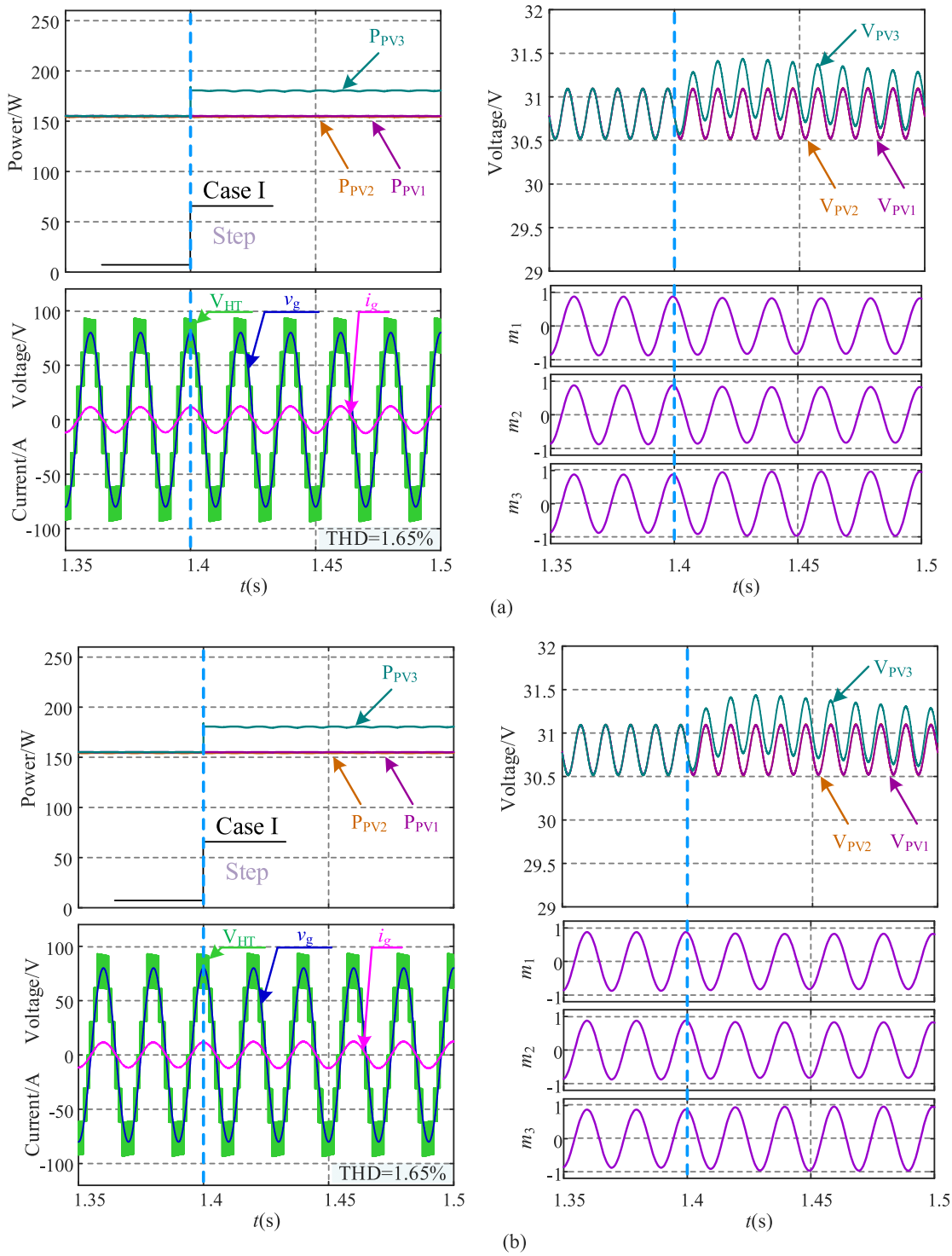


Fig. 19. Simulation results of output power and voltage of PV module, inverter output voltage, grid voltage, grid current and modulation waveform of each H-bridge unit under operation Case I with: (a) fundamental voltage reconstruction method; (b) third harmonic injection method.

Substituting (19) into (46), the expression of power routing range of the HMSCZS method could be obtained as shown in (47), at the bottom of the next page.

Similar to the first two methods, only the power routing range of the three-unit CHB PV grid-connected inverter is given here. For comparison, the power routing range based on the optimized third harmonic injection method is given here again. When $L^* = 5\%$ and $\xi = 10\%$, the PRS and PRF based on the HPWM power routing method is shown in Fig. 18. As depicted in the figure, compared with the method based on optimized third harmonic injection, the method based on HPWM significantly expands the PRS, and its PRF is as high as 36.77%. The relationship between the PRF based on the HPWM and $L^*$, $\xi$ is the same as the conclusion in the previous section and will not be repeated

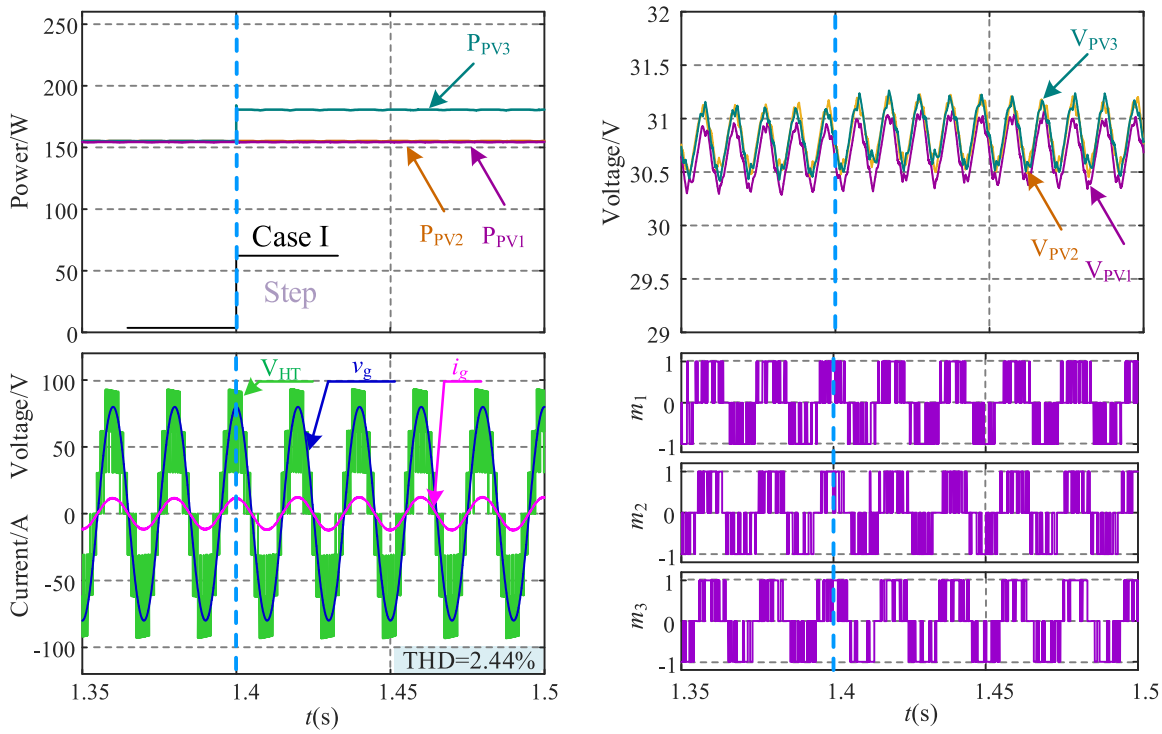


Fig. 20. Simulation results of output power and voltage of PV module, inverter output voltage, grid voltage, grid current and ratio of output voltage to dc-side voltage of each H-bridge unit under operation Case I with HPWM strategy.

TABLE I
PV MODULE PARAMETERS

| Symbol | Parameter | Value |
|---|---|---|
| $P_m$ | Peak power of PV module | 255W |
| $V_{oc}$ | Open circuit voltage of PV module | 37.61V |
| $V_{mp}$ | Max power voltage of PV module | 30.59V |
| $I_{sc}$ | Short circuit current of PV module | 8.90A |
| $I_{mp}$ | Max power current of PV module | 8.34A |

TABLE II
GRID AND INVERTER PARAMETERS

| Symbol | Parameter | Value |
|---|---|---|
| $C_i$ | DC-side capacitance | 28.2mF |
| $L_s$ | Filter inductance | 2mH |
| $V_G$ | Grid voltage peak value | 80V |
| $f_{grid}$ | Grid voltage frequency | 50Hz |
| $f_c$ | PWM frequency | 2500Hz |

here. The dc-side voltage utilization efficiency of each H-bridge unit can be effectively improved by adopting HPWM, thereby further expanding the power routing range of the system.

## V. SIMULATION RESULTS

To verify the validity of the abovementioned theoretical analyses, a single-phase seven-level CHB inverter is simulated in MATLAB/Simulink. The PV module under investigation is JAP6-60-255/4BB, with the specifications and equivalent circuit parameters mentioned in Table I. Inverter and grid parameters are given in Table II. For the sake of simplicity, the performance of the first power routing control method based on fundamental voltage reconstruction, the traditional third harmonic injection method, and HPWM strategy are compared in simulations.

### A. Case I ($\lambda_1 = 0.61$, $\lambda_2 = 0.61$, $\lambda_3 = 0.71$)

In the simulation, the ambient temperature is set to 25 °C, and the irradiance in initial of the PV module corresponding to each H-bridge unit is set to 600, 600, and 600 W/m$^2$, respectively. At $t = 1.4$ s, the irradiance of the third PV module is changed from 600 W/m$^2$ to 700 W/m$^2$ and the irradiance of others still remain unchanged. In this case, the fundamental modulation degree of each H-bridge unit is 0.82, 0.82, and 0.96, respectively. Fig. 19 shows the output power and voltage of each PV module, inverter output voltage, grid voltage, grid current, and modulation waveform of each H-bridge unit with the methods of fundamental voltage reconstruction and third harmonic injection. Fig. 20 shows the output power and voltage of PV module, inverter output voltage, grid voltage, grid current, and the ratio of output voltage to dc-side voltage of each H-bridge unit when HPWM strategy is adopted. When the

$$\begin{cases} \sqrt{1+\left(\frac{1}{n}\sum_{i=1}^{n}\lambda_i L^*\right)^2}\cos\left(\omega t+\arctan\left(\frac{1}{n}\sum_{i=1}^{n}\lambda_i L^*\right)\right) \le (1+\xi)\sqrt{1+(L^*)^2} \\ \frac{\lambda_i}{\sum_{i=1}^{n}\lambda_i}\sqrt{1+\left(\frac{1}{n}\sum_{i=1}^{n}\lambda_i L^*\right)^2}\cos\left(\omega t+\arctan\left(\frac{1}{n}\sum_{i=1}^{n}\lambda_i L^*\right)\right) \le \frac{4}{\pi}\frac{(1+\xi)\sqrt{1+(L^*)^2}}{n}, i=1,2,\ldots,n \end{cases} \tag{47}$$

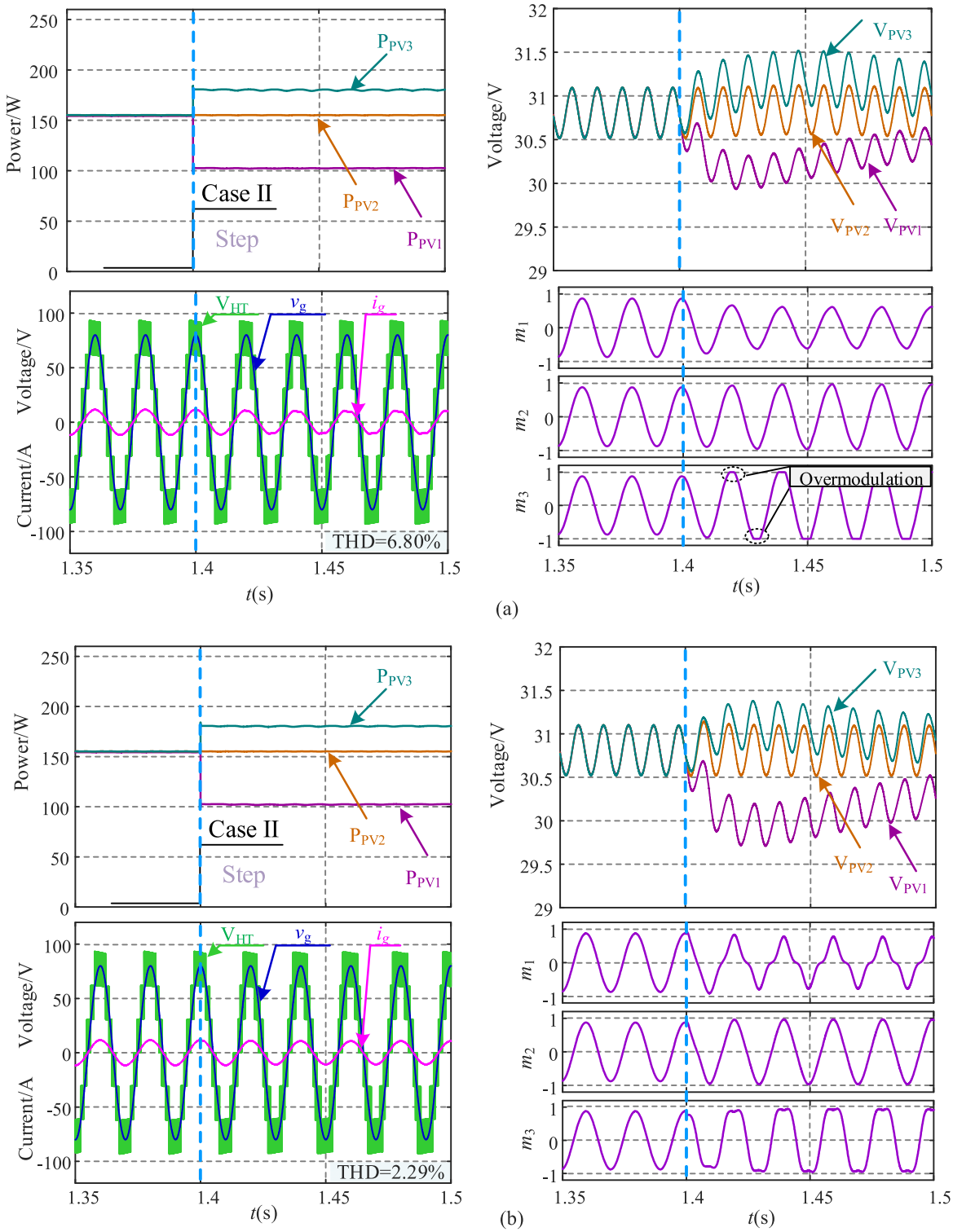


Fig. 21. Simulation results of output power and voltage of PV module, inverter output voltage, grid voltage, grid current, and modulation waveform of each H-bridge unit under operation Case II with: (a) fundamental voltage reconstruction method; (b) third harmonic injection method.

fundamental voltage reconstruction, third harmonic injection and HPWM methods are utilized, the maximum fundamental modulation degree of the H-bridge unit is 1, 1.155, and 1.27, respectively. Therefore, as depicted in Figs. 19 and 20, all the H-bridge units are free from overmodulation and the inverter can operate normally under these three methods. Under these three methods, the THD of grid current is 1.65%, 1.65%, and 2.44%, respectively.

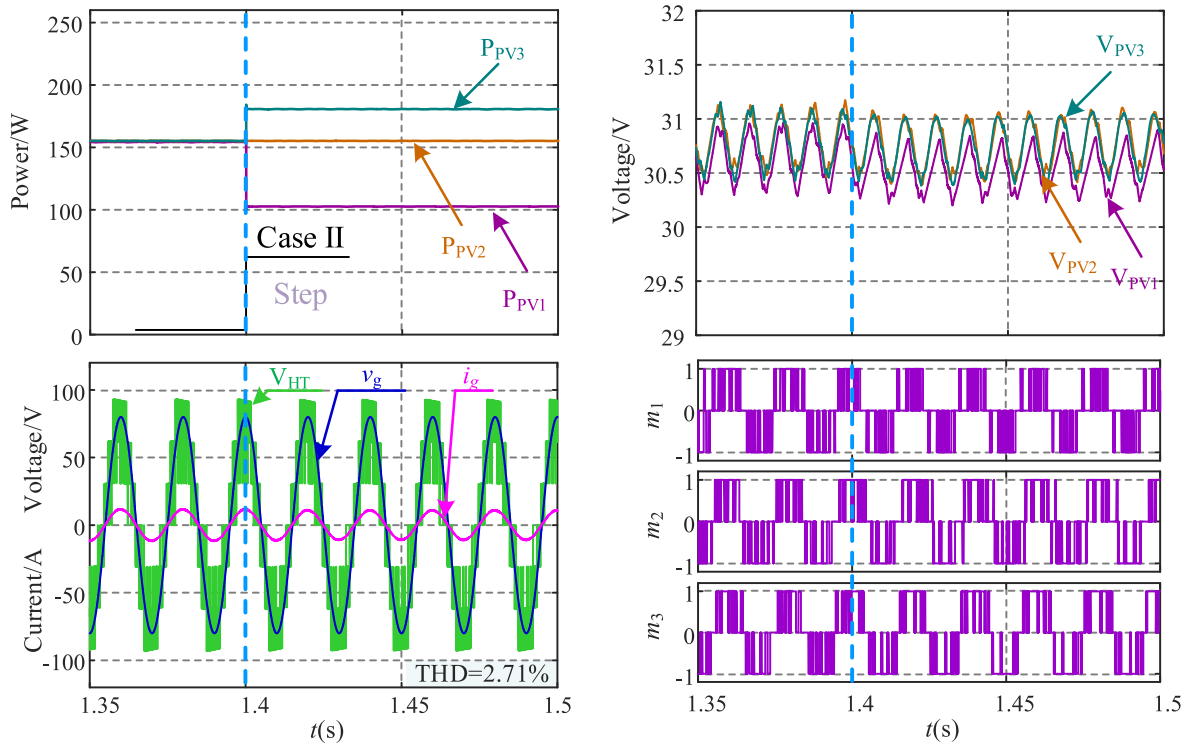


Fig. 22. Simulation results of output power and voltage of PV module, inverter output voltage, grid voltage, grid current, and ratio of output voltage to dc-side voltage of each H-bridge unit under operation Case II with HPWM strategy.

### *B. Case II ($\lambda_1 = 0.40$, $\lambda_2 = 0.61$, $\lambda_3 = 0.71$)*

In the simulation, the ambient temperature is set to 25 °C, and the irradiance in initial of the PV module corresponding to each H-bridge unit is set to 600, 600, and 600 W/m$^2$, respectively. At $t = 1.4$ s, the irradiance of the first PV module decreased to 400 W/m$^2$ from 600 W/m$^2$ while the irradiance of third PV module increased by 100 W/m$^2$. Fig. 21 (a) shows the output power and voltage of each PV module, inverter output voltage, grid voltage, grid current, and modulation waveform of each H-bridge unit using fundamental voltage reconstruction method, from which obvious harmonic distortion of grid current can be observed, with THD of 6.80% after $t = 1.4$ s. In this case, the fundamental modulation degree of each H-bridge unit is 0.61, 0.92, and 1.07, respectively, which is beyond the capability of the fundamental voltage reconstruction method. However, the third harmonic injection and HPWM methods shown in Figs. 21(b) and 22 can make each H-bridge work at their respective maximum power points, because the maximum fundamental modulation degree of the H-bridge unit using the two methods is 1.155 and 1.27, respectively. Therefore, all the H-bridge units are free from overmodulation and the inverter can operate normally under both methods. Under these two methods, the THD of grid current is 2.29% and 2.71%, respectively.

### *C. Case III ($\lambda_1 = 0.50$, $\lambda_2 = 0.61$, $\lambda_3 = 1$)*

In the simulation, the ambient temperature is set to 25 °C, and the irradiance in initial of the PV module corresponding to each H-bridge unit is set to 600, 600, and 600 W/m$^2$, respectively. At $t = 1.4$ s, the irradiance of the first PV module decreased to 500 W/m$^2$ from 600 W/m$^2$ while the irradiance of third PV module increased by 400 W/m$^2$. Fig. 23(a) and (b) shows the output power and voltage of each PV module, inverter output voltage, grid voltage, grid current, and modulation waveform of each H-bridge unit when the fundamental voltage reconstruction and third harmonic injection methods are utilized, respectively. It can be seen that the grid current has serious harmonic distortion after $t = 1.4$ s under both methods, and the THD is 26.31% and 8.89%, respectively. In this case, the fundamental modulation degree of each H-bridge unit is 0.62, 0.75, and 1.24, respectively, which exceeds the capability of the fundamental voltage reconstruction and third harmonic injection methods. However, HPWM method shown in Fig. 24 is still capable of dealing with this unequal power distribution condition, because the maximum fundamental modulation degree of the H-bridge unit using this method can reach 1.27. It can be seen from Fig. 24 that the third H-bridge unit is close to square wave modulation. Therefore, all the H-bridge units are free from overmodulation and the inverter can operate normally with this method. Under this method, the THD of grid current is 2.21%.

Finally, based on the abovementioned content, Table III is given in order to compare the characteristics of different control methods more intuitively. The design complexity, implementation complexity of each control method, the maximum modulation degree that each H-bridge module can achieve in the table. In addition, the PRFs of each power control method and the current THD under three simulation conditions is given when $n = 3$, $L^* = 5\%$, $\xi = 10\%$.

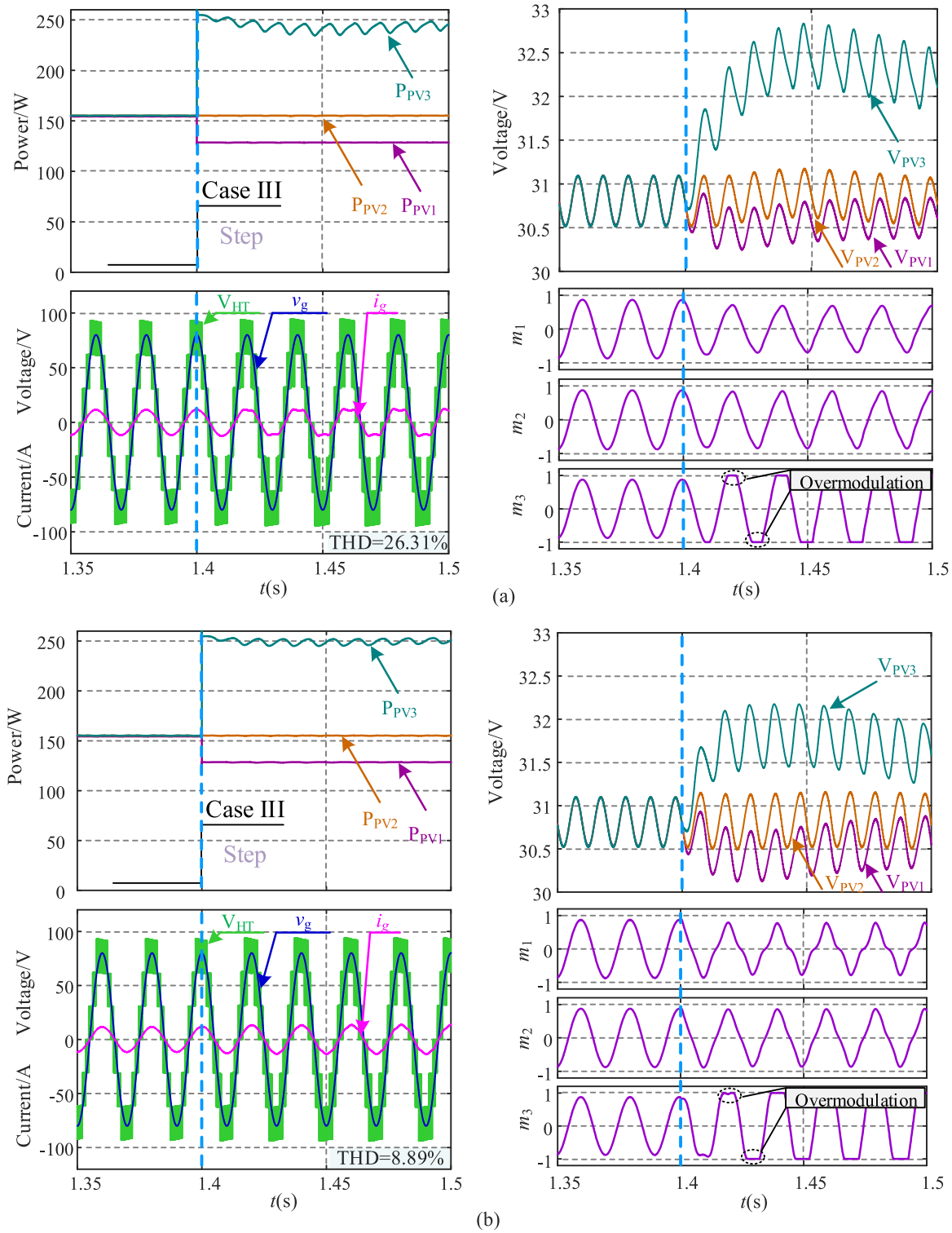


Fig. 23. Simulation results of output power and voltage of PV module, inverter output voltage, grid voltage, grid current, and modulation waveform of each H-bridge unit under operation Case III with: (a) fundamental voltage reconstruction method; (b) third harmonic injection method.

## VI. Conclusion

This article introduces several typical power routing control methods of single-phase CHB PV grid-connected inverter based on fundamental voltage reconstruction, third harmonic injection, and HPWM. At the same time, the expressions of their power routing ranges are mathematically deduced in detail, and their power routing capabilities are compared by qualitative index PRS and quantitative index PRF. The simulation results of a single-phase seven-level CHB PV grid-connected inverter verify the validity of the theoretical analyses.

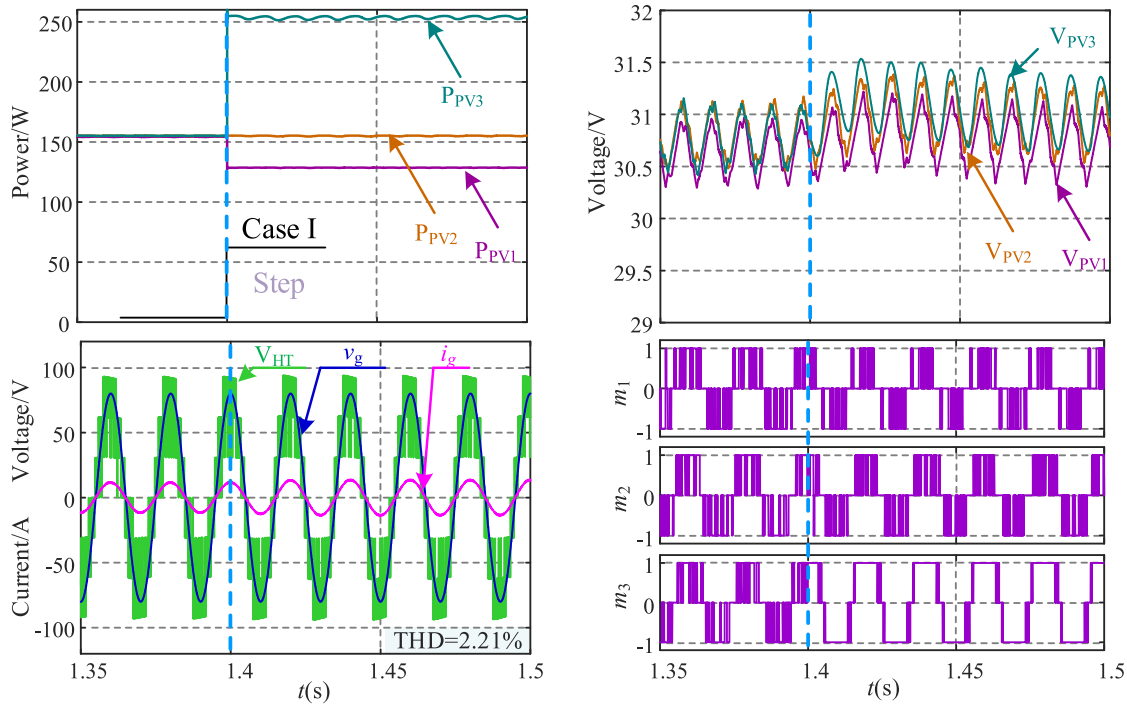


Fig. 24. Simulation results of output power and voltage of PV module, inverter output voltage, grid voltage, grid current, and ratio of output voltage to dc-side voltage of each H-bridge unit under operation Case II with HPWM strategy.

TABLE III
COMPREHENSIVE COMPARISON OF DIFFERENT CONTROL METHODS

| Method | Design complexity | Implementation complexity | Max modulation degree | Max PRF | Grid current THD | | |
|---|---|---|---|---|---|---|---|
| | | | | | Case I | Case II | Case III |
| Fundamental voltage reconstruction | Simple | Simple | 1 | 3.75% | 1.65% | 6.80% | 26.31% |
| Third harmonic injection | Medium | Medium | 1.155 | 20.37% | 1.65% | 2.29% | 8.89% |
| HPWM | Complex | Complex | 1.27 | 36.77% | 2.44% | 2.71% | 2.21% |

Based on the comparative study of several typical power routing control methods of single-phase CHB PV grid-connected inverter, the following conclusions can be drawn.

1) The power routing ranges of several typical power routing control methods are only related to the number $n$ of H-bridge unit, per unit value of filter inductor $L^*$, and the voltage overrating $\xi$. Under the premise that the number $n$ of H-bridge unit is constant, the change of $L^*$ has little effect on the power routing range, and as $\xi$ becomes larger, the power routing range increases significantly.
2) The power routing control method based on fundamental voltage reconstruction can be divided into three types according to the reactive power distribution method of each H-bridge unit. The PRSs of the three methods are very small, with only slight differences. When $n = 3$, $L^* = 5\%$, $\xi = 10\%$, PRFs of the three methods are 3.74%, 3.67%, and 3.75%, respectively.
3) Compared with the power routing control method based on fundamental voltage reconstruction, the traditional third harmonic injection method greatly expands the PRS, and its PRF is 19.79%. Based on the traditional third harmonic injection method, the optimized third harmonic injection method further expands the PRS, and its PRF is 20.37%.
4) Compared with the power routing control method based on the third harmonic injection, the HPWM strategy significantly expands the PRS, and its PRF is as high as 36.77%.

## REFERENCES

[1] X. Zhang, T. Zhao, W. Mao, D. Tan, and L. Chang, "Multilevel inverters for grid-connected photovoltaic applications: examining emerging trends," *IEEE Power Electron. Mag.*, vol. 5, no. 4, pp. 32–41, Dec. 2018.
[2] E. Babaei, C. Buccella, and M. Saeedifard, "Recent advances in multilevel inverters and their applications—part ii," *IEEE Trans. Ind. Electron.*, vol. 63, no. 12, pp. 7777–7779, Dec. 2016.
[3] X. Zhang, M. Wang, T. Zhao, W. Mao, Y. Hu, and R. Cao, "Topological comparison and analysis of medium-voltage and high-power direct-linked pv inverter," *CES Trans. Elect. Mach. Syst.*, vol. 3, no. 4, pp. 327–334, Dec. 2019.
[4] Y. Yu, G. Konstantinou, C. D. Townsend, R. P. Aguilera, and V. G. Agelidis, "Delta-connected cascaded h-bridge multilevel converters for large-scale photovoltaic grid integration," *IEEE Trans. Ind. Electron.*, vol. 64, no. 11, pp. 8877–8886, Nov. 2017.
[5] H. D. Tafti, A. I. Maswood, G. Konstantinou, C. D. Townsend, P. Acuna, and J. Pou, "Flexible control of photovoltaic grid-connected cascaded h-bridge converters during unbalanced voltage sags," *IEEE Trans. Ind. Electron.*, vol. 65, no. 8, pp. 6229–6238, Aug. 2018.

[6] R. Sharma and A. Das, "Extended reactive power exchange with faulty cells in grid-tied cascaded h-bridge converter for solar photovoltaic application," *IEEE Trans. Power Electron.*, vol. 35, no. 6, pp. 5683–5691, Jun. 2020.
[7] M. A. Rezaei, S. Farhangi, and H. Iman-Eini, "Extending the operating range of cascaded h-bridge based multilevel rectifier under unbalanced load conditions," in *Proc. IEEE Int. Conf. Power Energy*, Kuala Lumpur, Malaysia, 2010, pp. 780–785.
[8] A. Eskandari, V. Javadian, H. Iman-Eini, and M. Yadollahi, "Stable operation of grid connected cascaded h-bridge inverter under unbalanced insolation conditions," in *Proc. 3rd Int. Conf. Electric Power Energy Convers. Syst.*, Istanbul, 2013, pp. 1–6.
[9] Y. Ko, M. Andresen, G. Buticchi, M. Liserre, and L. Concari, "Multi-frequency power routing for cascaded h-bridge inverters in smart transformer application," in *Proc. IEEE Energy Convers. Congr. Expo.*, Milwaukee, WI, USA, 2016, pp. 1–7.
[10] M. Liserre, M. Andresen, L. Costa, and G. Buticchi, "Power routing in modular smart transformers: active thermal control through uneven loading of cells," *IEEE Ind. Electron. Mag.*, vol. 10, no. 3, pp. 43–53, Sep. 2016.
[11] V. Raveendran, G. Buticchi, A. Mercante, and M. Liserre, "Comparison of voltage control methods of chb converters for power routing in smart transformer," in *Proc. IEEE Energy Convers. Congr. Expo.*, Cincinnati, OH, USA, 2017, pp. 1652–1658.
[12] G. Buticchi, M. Andresen, M. Wutti, and M. Liserre, "Lifetime-based power routing of a quadruple active bridge dc/dc converter," *IEEE Trans. Power Electron.*, vol. 32, no. 11, pp. 8892–8903, Nov. 2017.
[13] M. Andresen, V. Raveendran, G. Buticchi, and M. Liserre, "Lifetime-based power routing in parallel converters for smart transformer application," *IEEE Trans. Ind. Electron.*, vol. 65, no. 2, pp. 1675–1684, Feb. 2018.
[14] V. Raveendran, M. Andresen, and M. Liserre, "Graph theory-based power routing in modular power converters considering efficiency and reliability," in *Proc. 44th Annu. Conf. IEEE Ind. Electron. Soc.*, Washington, DC, USA, 2018, pp. 1237–1242.
[15] V. Raveendran, M. Andresen, G. Buticchi, and M. Liserre, "Thermal stress based power routing of smart transformer with chb and dab converters," *IEEE Trans. Power Electron.*, vol. 35, no. 4, pp. 4205–4215, Apr. 2020.
[16] O. Alonso, P. Sanchis, E. Gubia, and L. Marroyo, "Cascaded h-bridge multilevel converter for grid connected photovoltaic generators with independent maximum power point tracking of each solar array," in *Proc. 34th Annu. Conf. Power Electron. Specialist*, Acapulco, Mexico, 2003, vol. 2, pp. 731–735.
[17] J. J. Negroni, F. Guinjoan, C. Meza, D. Biel, and P. Sanchis, "energy-sampled data modeling of a cascade h-bridge multilevel converter for grid-connected pv systems," in *Proc. IEEE Int. Power Electron. Congr.*, Puebla, 2006, pp. 1–6.
[18] S. Kouro, B. Wu, Á. Moya, E. Villanueva, P. Correa, and J. Rodríguez, "control of a cascaded h-bridge multilevel converter for grid connection of photovoltaic systems," in *Proc. 35th Annu. Conf. IEEE Ind. Electron.*, Porto, 2009, pp. 3976–3982.
[19] J. Chavarria, D. Biel, F. Guinjoan, C. Meza, and J. J. Negroni, "Energy-balance control of pv cascaded multilevel grid-connected inverters under level-shifted and phase-shifted pwms," *IEEE Trans. Ind. Electron.*, vol. 60, no. 1, pp. 98–111, Jan. 2013.
[20] Q. Huang, M. Wang, W. Yu, and A. Q. Huang, "Power-weighting-based multiple input and multiple output control strategy for single-phase pv cascaded h-bridge multilevel grid-connected inverter," in *Proc. IEEE Appl. Power Electron. Conf. Expo.*, Charlotte, NC, USA, 2015, pp. 2148–2153.
[21] A. Dell'Aquila, M. Liserre, V. G. Monopoli, and P. Rotondo, "Overview of pi-based solutions for the control of dc buses of a single-phase h-bridge multilevel active rectifier," *IEEE Trans. Industry Appl.*, vol. 44, no. 3, pp. 857–866, May/Jun. 2008.
[22] E. Villanueva, P. Correa, J. Rodriguez, and M. Pacas, "Control of a single-phase cascaded h-bridge multilevel inverter for grid-connected photovoltaic systems," *IEEE Trans. Ind. Electron.*, vol. 56, no. 11, pp. 4399–4406, Nov. 2009.
[23] Y. Liu, B. Ge, H. Abu-Rub, and F. Z. Peng, "An effective control method for quasi-z-source cascade multilevel inverter-based grid-tie single-phase photovoltaic power system," *IEEE Trans. Ind. Informat.*, vol. 10, no. 1, pp. 399–407, Feb. 2014.
[24] T. Zhao, G. Wang, S. Bhattacharya, and A. Q. Huang, "Voltage and power balance control for a cascaded h-bridge converter-based solid-state transformer," *IEEE Trans. Power Electron.*, vol. 28, no. 4, pp. 1523–1532, Apr. 2013.
[25] Y. Sun, J. Zhao, and Z. Ji, "Control strategy of dc voltage balance and power equilibrium for grid-connected cascaded h-bridge converters," *Electric Power Autom. Equipment*, vol. 34, no. 1, pp. 55–60, Jan. 2013.
[26] S. Wang, J. Zhao, X. Yao, and Y. Sun, "Power balanced controlling of cascaded inverter for grid-connected photovoltaic systems under unequal irradiance conditions," *Trans. China Electrotechnical Soc.*, vol. 28, no. 12, pp. 251–261, Dec. 2013.
[27] C. Zhang, J. Zhou, and C. Du, "review of control strategies of single-phase cascaded h-bridge multilevel inverter for grid-connected photovoltaic systems," *J. Power Supply*, vol. 15, no. 1, pp. 1–8, Jan. 2017.
[28] Y. Ko, M. Andresen, G. Buticchi, and M. Liserre, "Power routing for cascaded h-bridge converters," *IEEE Trans. Power Electron.*, vol. 32, no. 12, pp. 9435–9446, Dec. 2017.
[29] T. Zhao, X. Zhang, W. Mao, F. Wang, J. Xu, and Y. Gu, "An optimized third harmonic compensation strategy for single-phase cascaded h-bridge photovoltaic inverter," *IEEE Trans. Ind. Electron.*, vol. 65, no. 11, pp. 8635–8645, Nov. 2018.
[30] X. Zhang *et al.*, "A grid-supporting strategy for cascaded h-bridge pv converter using vsg algorithm with modular active power reserve," *IEEE Trans. Ind. Electron.*, to be published.
[31] Y. Ko, V. Raveendran, M. Andresen, and M. Liserre, "thermally compensated discontinuous modulation for mvac/lvdc building blocks of modular smart transformers," *IEEE Trans. Power Electron.*, vol. 35, no. 1, pp. 220–231, Jan. 2020.
[32] Y. Ko, V. Raveendran, M. Andresen, and M. Liserre, "Discontinuous modulation based power routing for modular smart transformers," in *Proc. IEEE Energy Convers. Congr. Expo.*, Portland, OR, USA, 2018, pp. 1084–1090.
[33] Y. Ko, M. Andresen, G. Buticchi, J. Lee, and M. Liserre, "modulation strategy for highly reliable cascade h-bridge inverter based on discontinuous pwm," in *Proc. IEEE Appl. Power Electron. Conf. Expo.*, Tampa, FL, USA, 2017, pp. 3241–3246.
[34] Y. Ko, M. Andresen, G. Buticchi, and M. Liserre, "Discontinuous-modulation-based active thermal control of power electronic modules in wind farms," *IEEE Trans. Power Electron.*, vol. 34, no. 1, pp. 301–310, Jan. 2019.
[35] H. Iman-Eini, J. Schanen, S. Farhangi, and J. Roudet, "A modular strategy for control and voltage balancing of cascaded h-bridge rectifiers," *IEEE Trans. Power Electron.*, vol. 23, no. 5, pp. 2428–2442, Sep. 2008.
[36] A. Keshavarzian and H. Iman-Eini, "A redundancy-based scheme for balancing dc-link voltages in cascaded h-bridge rectifiers," *IET Power Electron.*, vol. 6, no. 2, pp. 235–243, Feb. 2013.
[37] M. Moosavi, G. Farivar, H. Iman-Eini, and S. M. Shekarabi, "a voltage balancing strategy with extended operating region for cascaded h-bridge converters," *IEEE Trans. Power Electron.*, vol. 29, no. 9, pp. 5044–5053, Sep. 2014.
[38] M. Coppola, F. Di Napoli, P. Guerriero, D. Iannuzzi, S. Daliento, and A. Del Pizzo, "An fpga-based advanced control strategy of a gridtied pv chb inverter," *IEEE Trans. Power Electron.*, vol. 31, no. 1, pp. 806–816, Jan. 2016.
[39] M. Miranbeigi and H. Iman-Eini, "Hybrid modulation technique for grid-connected cascaded photovoltaic systems," *IEEE Trans. Ind. Electron.*, vol. 63, no. 12, pp. 7843–7853, Dec. 2016.
[40] T. Zhao, X. Zhang, W. Mao, F. Wang, J. Xu, and Y. Gu, "A modified hybrid modulation strategy for suppressing dc voltage fluctuation of cascaded h-bridge photovoltaic inverter," *IEEE Trans. Ind. Electron.*, vol. 65, no. 5, pp. 3932–3941, May 2018.
[41] Y. Yu, G. Konstantinou, C. D. Townsend, and V. G. Agelidis, "Comparison of zero-sequence injection methods in cascaded h-bridge multilevel converters for large-scale photovoltaic integration," *IET Renewable Power Gener.*, vol. 11, no. 5, pp. 603–613, May 2017.

**Siwei Yang** was born in Anhui, China, in 1997. He received the B.S. degree in electrical engineering from the School of Information and Control Engineering, China University of Petroleum, Qingdao, China, in 2018. He is currently working toward the M.S. degree in electric engineering and automation with the Hefei University of Technology, Hefei, China.

His current research interests include the modeling and control of power converters and stability analysis of grid-connected inverters.

**Xing Zhang** (Senior Member, IEEE) was born in Shanghai, China, in 1963. He received the B.S., M.S., and Ph.D. degrees in electrical engineering and automation from the Hefei University of Technology, Hefei, China, in 1984, 1990, and 2003, respectively.

Since 1984, he has been a Faculty Member with the School of Electric Engineering and Automation, Hefei University of Technology, where he is currently a Professor and also serves as the Chief of National and Local Joint Engineering Laboratory for Renewable Energy Access to Grid Technology. He is also with the Photovoltaic Engineering Research Center of the Ministry of Education. His main research interests include photovoltaic generation technologies, wind power generation technologies, and distributed generation systems.

**Wang Mao** was born in Anhui, China, in 1992. He received the B.S. degree in electrical engineering and automation from the Anhui University, Hefei, China, in 2013, and the Ph.D. degree in electrical engineering from the Hefei University of Technology, Hefei, China, in 2020.

He is currently an Engineer with Shanghai Institute of Space Power-Sources, Shanghai. His current research interests include photovoltaic generation technologies and the modeling and control of power converters.

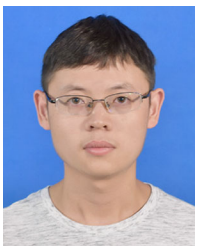

**Yuhua Hu** was born in Anhui, China, in 1994. He received the B.S. degree from the School of Electrical Engineering and Automation, Anhui University, Hefei, China, in 2017, and the M.S. degree from the Hefei University of Technology, Hefei, China, in 2020, both in electrical engineering.

His current research interests include the modeling and control of power converters and photovoltaic generation technologies.

**Mingda Wang** was born in Anhui, China, in 1996. He received the B.S. degree in electrical engineering in 2017 from the School of Electrical Engineering and Automation, Hefei University of Technology, Hefei, China, where he is currently working toward the Ph.D. degree in electric engineering and automation.

His current research interests include the control of power converters and photovoltaic generation technologies.

**Fusheng Wang** (Member, IEEE) was born in Anhui, China, in 1976. He received the B.S. degree in electric engineering and automation from the Hefei University of Technology, Hefei, China, in 1998, and the Ph.D. degree in nuclear science and engineering from the Institute of Plasma Physics Chinese Academy of Sciences, Hefei, China, in 2005.

In 2006, he was with the Faculty of the School of Electric Engineering and Automation, Hefei University of Technology, where he is currently an Associate Professor. His current research interests include control of multilevel converters, photovoltaic generation technologies, and wireless power transmission.

**Renxian Cao** was born in Zhejiang, China, in 1968. He received the B.S. and M.S. degrees in electric engineering and automation from the Hefei University of Technology, Hefei, China, in 1990 and 1993, respectively.

He is currently General Manager with Sungrow Power Supply Co., Ltd., Hefei, China, and a Professor with the School of Electric Engineering and Automation, Hefei University of Technology. His main research interests include photovoltaic generation technologies, wind power generation technologies, and distributed generation system.